Phase transformations in cast superaustenitic stainless steels

by

Nathaniel Steven Lee Phillips

A thesis submitted to the graduate faculty

in partial fulfillment of the requirements for the degree of

MASTER OF SCIENCE

Major: Materials Science and Engineering

Program of Study Committee:
L. Scott Chumbley, Co-major Professor
Brian Gleeson, Co-major Professor
Frank E. Peters

Iowa State University

Ames, Iowa

2006

TABLE OF CONTENTS

ABSTRACT

Superaustenitic stainless steels constitute a group of Fe-based alloys that are compositionally balanced to have a purely austenitic matrix and exhibit favorable pitting and crevice corrosion resistant properties and mechanical strength. However, intermetallic precipitates such as sigma (σ) and Laves can form during casting or exposure to high-temperature processing, which degrade the corrosion and mechanical properties of the material. The goal of this study was to accurately characterize the solid-solid phase transformations seen in cast superaustenitic stainless steels. Heat treatments were performed to understand the time and temperature ranges for intermetallic phase formations in alloys CN3MN and CK3MCuN. Microstructures were characterized using scanning electron microscopy (SEM), transmission electron microscopy (TEM), and energy and wavelength dispersive spectroscopy (EDS, WDS). The equilibrium microstructures, composed primarily of sigma and Laves within purely austenitic matrices, showed slow transformation kinetics. Factors that determine the extent of transformation, including diffusion, nucleation, and growth, are discussed.

CHAPTER 1. GENERAL INTRODUCTION

Superaustenitic stainless steels are a group of Fe-based alloys that exhibit favorable pitting and crevice corrosion resistant properties and mechanical strength. These alloys are especially designed for highly corrosive environments at elevated temperatures. [1-5] The favorable corrosion resistant properties are attributed to the high alloy content of Cr, Mo, and N, which produce a high pitting resistance equivalent number (PREN)[11], where:

$$(PREN) = \%Cr + 3.3 \times \% Mo + 17 \times \% N \qquad \textbf{Equation 1}$$

These alloys are also compositionally balanced with the addition of Ni to ensure that the material remains completely austenitic.[12]

When exposed to elevated temperatures for long periods of time, large amounts of precipitates, including carbides, nitrides and intermetallic phases, can form.[1-5] The most commonly observed secondary phases include $M_{23}C_6$ carbide, and intermetallic sigma, chi, and Laves phases.[1-5] Other less common secondary phases found in some superaustenitic alloys include M_6C, π, R and Cr_2N.[1-5] High amounts of these phases degrade the corrosion resistance and mechanical properties of the stainless steel.

There has been a large amount of research on the mechanical and corrosion resistant properties of superaustenitic stainless steels.[1-2,4-5] However, little work has been done on determining the transformation kinetics of the matrix to secondary phases as a function of time and temperature, and what has been done relates predominantly to wrought alloys.[3] Differences in the phase transformation kinetics between cast and wrought alloys, which are

presumably due to differences in the nominal composition, have been documented.[6] The focus of this study is to examine the transformation behavior of cast superaustenitic steels, particularly in regards to the formation of the σ and Laves phases, since they appear to be the most abundant and most detrimental to mechanical properties and corrosion resistance.[6]

The transformation kinetics and phase constituents that occur due to isothermal holds and quenching were analyzed with optical and scanning electron microscopy techniques in order to determine phase percentages. Number densities were also determined for all heat treatments to further understand the phase transformations of sigma and Laves. *Thermo-Calc*, a thermodynamic software program which uses appropriate thermodynamic databases to determine such things as driving force and equilibrium phase percentages and compositions, was used to try to predict equilibrium conditions.

CHAPTER 2. LITERATURE REVIEW

2.1. Phase Equilibrium Properties of Fe-based Alloys

2.1.1. Fe-C Alloys (Fe-Fe_3C System)

In order to understand the transformation behavior of superaustenitic stainless steels, it is necessary to understand the Fe-Fe_3C system upon which they are based. Carbon steels have long been known for their ease of production and favorable combination of mechanical properties as a result of casting, machining and heat treating. However, plain-carbon steels are susceptible to corrosion. The corrosion process in steels can be slowed with alloying additions, such a Cr.

The Fe-Fe_3C phase diagram is presented in Figure 1. Pure Fe is able to form austenitic and ferritic phases as a result of cooling from its melting temperature(~1540°C). The Fe initially forms δ-ferrite upon cooling, which has a body-centered cubic (BCC) lattice structure. At ~1395°C, the lattice structure shifts from BCC to face-centered cubic (FCC). The resulting phase is termed austenite (γ). Further cooling to ~912°C will cause the lattice structure to shift back to BCC and form α-ferrite.

The transformation between these three phases is affected by cooling rate and composition. The low temperature transformation from γ to α may be prevented from happening if the cooling rate is fast enough. In this case, the shearing of the FCC lattice causes a body-centered tetragonal (BCT) lattice to form. This resulting phase is called martensite (γ′), which has a high hardness and low ductility due to its stressed lattice structure.

The intermetallic compound Fe_3C, which is called cementite, exists at 6.67 wt% C. Cementite has an orthorhombic lattice structure and is brittle and hard. An eutectoid reaction occurs at 727°C, where γ transforms to $\alpha + Fe_3C$. The reaction results in the formation of a lamellar $\alpha + Fe_3C$ structure termed pearlite. The soft ferrite combined with the hard cementite creates a microstructure with favorable mechanical properties.

The addition of alloying elements also affects the stability of phases in the Fe-C system. The formation of γ is stabilized by the additions of Ni, C, Mn, and N, while α is stabilized by the additions of Cr, Si, Mo, and Nb. These elements affect the phase stability so that the respective phases can form over wider composition and temperature ranges than what is found in the Fe-C system.

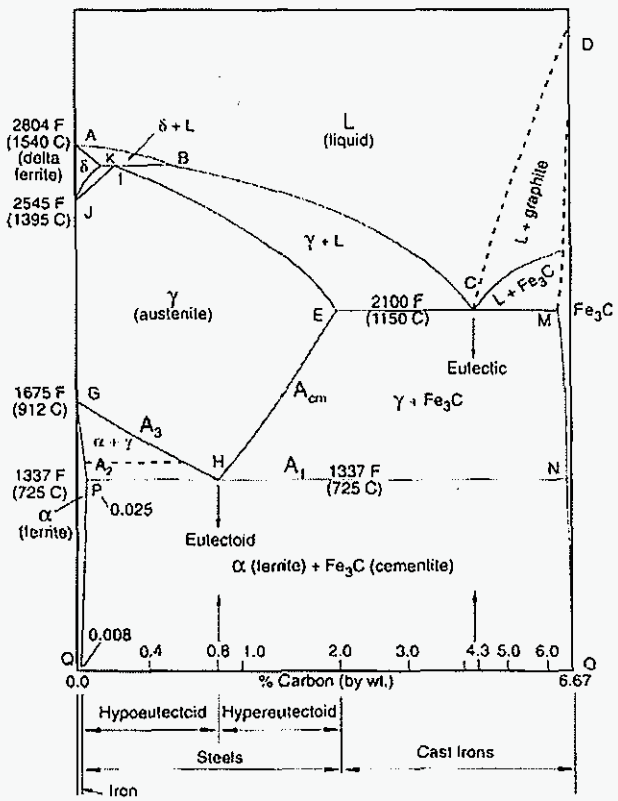

Figure 1 Fe-Fe_3C Phase Diagram[7]

2.1.2 Stainless Steel

Stainless steels are Fe-based alloys that have at least 12% Cr[7], which makes them oxidation resistant. These alloys are known as "stainless" due to the ability to prevent rust, or Fe_2O_3, from forming. A passive Cr-rich oxide surface protects the underlying metal from corrosion. Other alloying additions, which include Ni, Mo, Cu, Ti, Al, Si, Nb, N and W, are added to improve the mechanical and corrosion resistant properties of stainless steels. Upon solidification, stainless steels generally have either a ferritic or austenitic microstructure, or sometimes both. Stainless steels are separated into five major groups based on their composition and crystal structure: ferritic, austenitic, martensitic, duplex, and precipitation-hardened alloys.

Several secondary precipitates, including nitrides, carbides, and intermetallics, are also known to form in highly alloyed steels. Formulas, crystal structures, and formation temperatures of these secondary phases are listed in Table 1.

Table I Typical phases in high alloyed stainless steels[8]

Stainless Steel*	Phase	Symbol	Type	Formula	Temperature Range	Structure	Lattice Constants
D	chromium carbide	–	M_7C_3	$(Cr,Fe,Mo)_7C_3$	950-1050°C	orthorhombic	a=4.52, b=6.99, c=12.11
A, D, F	chromium carbide	–	$M_{23}C_6$	$(Cr,Fe,Mo)_{23}C_6$	600-950°C	cubic	a=10.57-10.68
A, D, F	chromium carbide	–	M_6C	$(Cr,Fe,Mo,Cb)_6C$	700-950°C	cubic	a= 10.93-11.28
D, F	chromium nitride	–	M_2N	$(Cr,Fe)_2N$	650-950°C	hexagonal	a=2.77, c=4.46
D	chromium nitride	–	MN	CrN	–	cubic	–
D	Fe-Mo nitride	–	M_3N	$Fe_2Mo_2N_4$	550-600°C	–	a = 6.47
A	Nb-Cr nitride	Z	MN	(NbCr)N	700-1000°C	tetragonal	a=3.03, c=7.37
F	titanium carbo-nitride	–	MC	Ti(CN)	700°C-m.p.	cubic	a=4.32-4.24
F	niobium carbo-nitride	–	MC	Nb(CN)	700°C-m.p.	cubic	a=4.42-4.38
A, D, F	Sigma	σ	AB	(Fe,Cr,Mo,Ni)	550-1050°C	tetragonal	a=8.79, c=4.54
A, D, F	Chi	χ	$A_{48}B_{10}$	$Fe_{36}Cr_{12}Mo_{10}$ $(FeNi)_{36}Cr_{18}(TiMo)_4$	600-900°C	cubic	a=8.86-8.92
D, F	Alpha prime	α'	-	CrFe(Cr 61-83%)	350-550°C	cubic	a=2.877
A, D, F	Laves	η	A_2B	$(FeCr)_2(Mo,Nb,Ti,Si)$	550-900°C	hexagonal	a=4.73-4.82, c=7.26-7.85
D, F	R	R	–	(Fe,Mo,Cr,Ni)	550-650°C	rhombohedral	a=10.903, c=19.347
D	Tau	τ	–	–	550-650°C	orthorhombic	a=4.05, b=4.84, c=2.86

*Code: A = Austenitic, D = Duplex, F = Ferritic

2.1.2.1 Austenitic Stainless Steels

Austenitic stainless steels constitute the largest group of stainless steels when considering the number of alloys. Upon solidification, this group of alloys generally has an FCC austenite matrix. However, some alloys in this group can contain up to 30% ferrite. Austenite stabilizers Ni, Cr, Mn and N are added to the Fe-Cr binary system to obtain such microstructures. Austenitic stainless steels generally contain between 16 and 25% Cr and up to 35% Ni and 15% Mn.

Molybdenum is added to increase the corrosion resistance of these alloys in seawater and chloride solutions. Nitrogen can be added to increase the yield strength by decreasing the tendency of carbide formation. Figure 2 shows the effect of N on tensile and yield strength and elastic modulus of cast austenitic stainless steel alloy CF3.

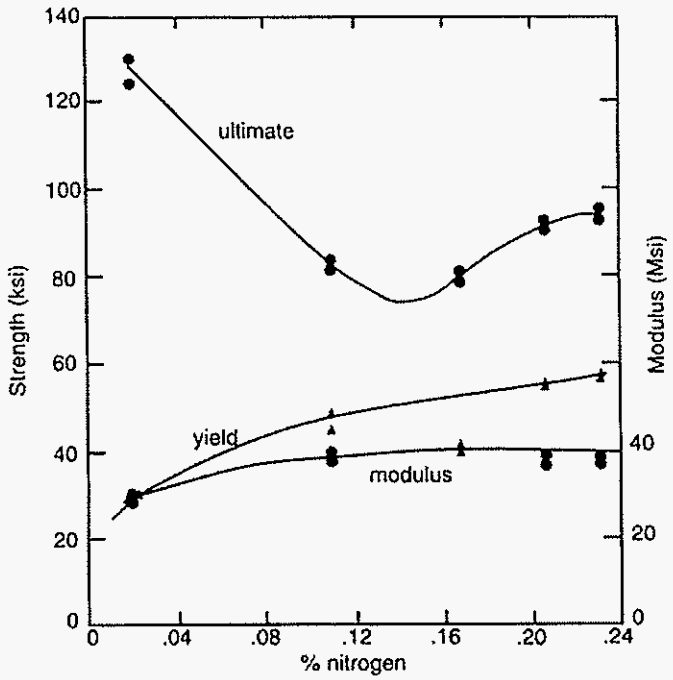

Figure 2 Nitrogen effect on the tensile and yield strength and the elastic modulus of cast austenitic alloy CF3[7]

Machining superaustenitic alloys can be difficult. Cold working is the only way to harden austenitic stainless steels, as they are not hardened by heat treatment. During cold working, Cr-rich precipitates can form along the grain boundaries, making these alloys susceptible to intergranular corrosion. The critical temperature for the formation of Cr-rich precipitates is between 400 and 850°C. Selenium can be added to assist with the machining of these alloys; however, selenium inclusions reduce the pitting resistance of the material.

2.1.2.2. Superaustenitic Stainless Steels

Superaustenitic stainless steels are a sub-group of austenitic stainless steels that contain high amounts of Mo, Ni, and sometimes N. Typical composition ranges for superaustenitic stainless steels is presented in Table II. The increased Ni content ensures that upon solidification these alloys have a completely austenitic microstructure. These alloys are specifically designed for highly corrosive environments, and have a PREN number that ranges from 28.3 to 64.3.[9] The high Ni amounts improve stress-corrosion-cracking resistance. The high Mo and N amounts improve pitting and crevice corrosion resistance, while a summary of the physical properties of superaustenitic stainless steels is presented in Table III.

Table II Typical composition ranges for superaustenitic stainless steels[10]

Alloying Element	Composition, wt%
Cr	20 - 26
Ni	18 – 26
Mo	5 – 7
Cu	0.5 – 4.0
N	0.10 – 0.25
C	0.020 – 0.035 (max)
Fe	bal

Table III Representative physical properties for superaustenitic stainless steels[9]

Property	Range	Average
Density, (20°C), (gm/cm^3)	7.98 - 8.2	8.05
Thermal Expansion (20-100°C)($10^{-6}\cdot K^{-1}$)	14.3 - 16.5	15.2
Electrical Resistivity (20°C), ($\mu\cdot\Omega\cdot cm$)	80 - 108	93
Thermal Conductivity (20°C), ($W\cdot m^{-1}\cdot K^{-1}$)	11.4 - 16	12.9
Specific Heat (20°C), ($J\cdot kg^{-1}\cdot K^{-1}$)	440 - 510	480
Modulus of Elasticity (20°C), (GPa)	186 - 200	193

When stainless alloys are exposed to elevated temperatures, intermetallic precipitates and carbides often form. The most prominent of these precipitates are the σ, χ, and Laves phases. Precipitation of these phases can lead to the depletion of Cr and Mo in adjacent areas, causing susceptibility to pitting and intergranular corrosion. Further details regarding the metallurgy, properties, alloying effects, and phase equilibrium of superaustenitic stainless steels will be discussed in detail later in this chapter.

2.2 Solid State Phase Transformation

2.2.1. Factors Affecting Phase Transformations

2.2.1.1 Diffusion

Solid state phase transformations depend mostly on atomic movement; thus, diffusion is used to describe the transformation kinetics. There are two general types of diffusion that lead to solid state transformation: interstitial and substitutional. The movement of smaller interstitial atoms between larger atoms is called interstitial diffusion. In substitutional diffusion atoms move in a direction opposite of a defect mechanism, such as a grain boundary or vacancy.

Interstitial diffusion can be described as a random jump process. An interstitial atom will jump to a neighboring interstitial when its thermal energy can overcome the strain barrier energy of the lattice. The number of jumps per second is best described by Fick's 1st Law as presented in Equation 2.

$$J = -D\frac{dc}{dx} \qquad \textbf{Equation 2}$$

In this equation, D is the diffusion coefficient typically with units cm^2/sec, and dc/dx is the concentration gradient as a function of distance. The diffusion coefficient of a specific atom exponentially increases with temperature and is generally proportional to the inverse of the atomic weight.

Fick's 1st Law is only valid for steady state conditions. However, concentration most often varies with both distance and time. Fick's 2nd Law describes how diffusion of the atoms occurs under non-steady state conditions, as presented in Equation 3.

$$\frac{\partial c}{\partial t} = \frac{\partial}{\partial x}\left(D\frac{\partial c}{\partial x}\right) \qquad \textbf{Equation 3}$$

The diffusion coefficient is also dependent on the defect concentration in the lattice. In substitutional diffusion an atom can only jump if there is a vacant site at an adjacent lattice position. In order for this to happen, the vacancy must be moving in the opposite direction of the atomic diffusion. For a binary system with species A and B, Fick's 2nd Law for substitutional diffusion becomes:

$$\frac{\partial C_A}{\partial t} = \frac{\partial}{\partial x}\left(\tilde{D}\frac{\partial C_A}{\partial x}\right) \qquad \textbf{Equation 4}$$

In this equation, $\tilde{D}$, the interdiffusion coefficient, equals $X_B D_A + X_A D_B$ where X_A and X_B are mole fractions of A and B, respectively.

2.2.1.2. Precipitate Nucleation

Nucleation, the formation of small groups of atoms into nuclei, is the first step of solid state phase transformation. Nucleation in solids is predominately heterogeneous. Nucleation is controlled by the change in the Gibb's free energy of a system. There are four contributions associated with the free energy change during heterogeneous nucleation[11]:

1. The creation of nuclei with volume V will cause a volume free energy reduction of $V\Delta G_v$.
2. New interfaces with area A within the matrix with interface energy γ will increase the free energy by A γ.
3. A strain field will result due to a misfit between the new nuclei, and the matrix. This causes a volumetric strain energy ΔG_s, which increases the free energy.
4. The destruction of a defect can result due to the formation of nuclei and decreases the free energy of the system by ΔG_d. (This contribution is excluded in homogeneous nucleation.)

Thus, the total free energy for heterogeneous nucleation is given by:

$$\Delta G = -V(\Delta G_v - \Delta G_s) + A\gamma - \Delta G_d \qquad \textbf{Equation 5}$$

If the variation of γ with interface orientation is ignored and a spherical nucleus assumed, then

$$\Delta G = -\tfrac{4}{3}\pi r^3(\Delta G_v - \Delta G_s) + 4\pi r^2\gamma \qquad \textbf{Equation 6}$$

for homogeneous nucleation. This equation is graphed as function of r in Figure 3. The critical size of a nucleus, r*, is associated with the maximum excess free energy, or activation energy barrier, ΔG*. Differentiation of Equation 6 would yield equations for r* and ΔG*:

$$r^* = \frac{2\gamma}{(\Delta G_v - \Delta G_s)} \qquad \textbf{Equation 7}$$

$$\Delta G^* = \frac{16\pi\gamma^3}{3(\Delta G_v - \Delta G_s)^2} \qquad \textbf{Equation 8}$$

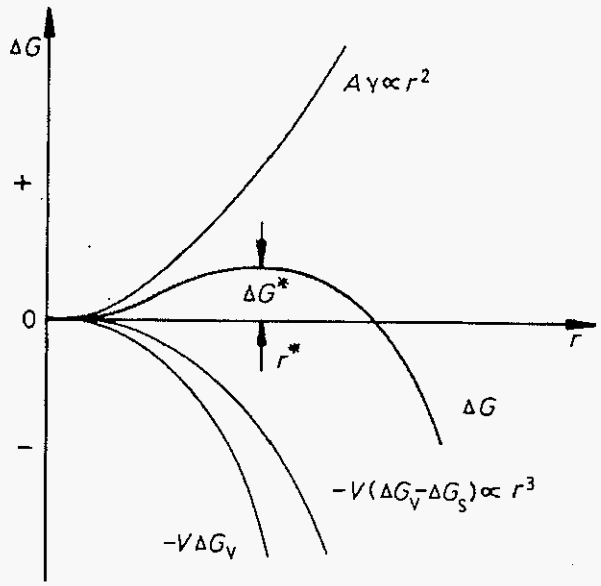

Figure 3 ΔG as a function of r for a homogeneous nucleus[11]

The homogeneous nucleation rate, N_{hom}, can be written as a function of how fast a critical sized nuclei can receive an atom from the matrix and the concentration of a critical sized nuclei, C*, where

$$C^* = C_o \exp(-\Delta G^*/kT) \qquad \textbf{Equation 9}$$

In Equation 9, C_o is the composition of homogeneous nucleation sites. This is determined by how fast diffusion occurs and the surface area of the nucleus. This speed can be written as $\omega\exp((-\Delta G_m/kT)$, where ω is a factor that includes the vibration frequency of the atoms and the area of the critical nucleas and ΔG_m is the activation energy for atomic migration.[11] Thus,

$$N_{hom}= \omega C_o \exp(-\Delta G^*/kT) \exp((-\Delta G_m/kT) \qquad \textbf{Equation 10}$$

The optimum shape of nuclei is that in which the interfacial energy is at a minimum. Thus, the optimum shape on an incoherent grain boundary would be two hemispherical caps, as presented in Figure 4. Figure 5 also shows critical nuclei shapes on a grain edge and grain corner.

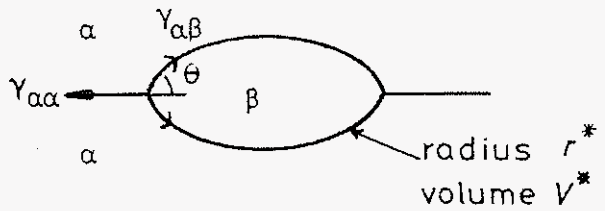

Figure 4 Critical nucleus size (V*) for grain boundary nucleation[11]

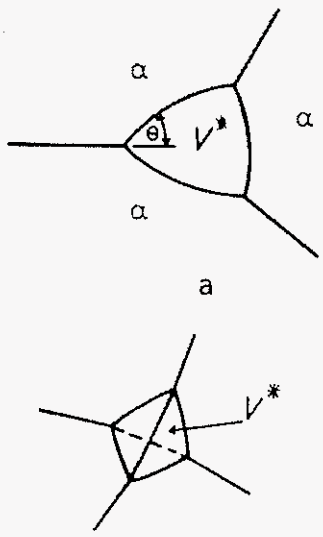

Figure 5 Critical nuclei shape for precipitation along a) grain edge and b) grain corner[11]

Defects such as grain boundaries, stacking faults and dislocations are energetically favorable places for precipitates to nucleate. This is why heterogeneous nucleation happens at a higher rate than homogenous nucleation. Grain boundaries are pathways for rapid diffusion when compared to the lattice. Therefore, nuclei form much faster along the grain boundaries than they do in the matrix, as is presented by a comparison of the ratio of heterogeneous and homogenous activation energies with nuclei size in Figure 6. The heterogeneous nucleation rate, N_{het}, can be written as

$$N_{het} = \omega C_1 \exp(-\Delta G^*/kT) \exp((-\Delta G_m/kT) \quad \textbf{Equation 11}$$

where C_1 is the concentration of heterogeneous nucleation sites. ΔG^* for heterogeneous nucleation is related to ΔG^* for homogeneous nucleation by a structure factor, $S(\Theta)$, where

$$\Delta G^*_{het} = \Delta G^*_{hom} S(\Theta) \quad \textbf{Equation 12}$$

$$S(\Theta) = \frac{2 - 3\cos\Theta - \cos^3\Theta}{2} \quad \textbf{Equation 13}$$

In Equation 13, Θ is the contact angle of a precipitate along as grain boundary, as presented in Figure 4. A ratio of heterogeneous to homogeneous nucleation rates can be determined so that

$$\frac{N_{het}}{N_{hom}} = \frac{C_1}{C_o} \exp\left(\frac{\Delta G^*_{hom} - \Delta G^*_{het}}{kT}\right) \quad \textbf{Equation 14}$$

Grain boundary nucleation gives the relationship

$$\frac{C_1}{C_o} = \frac{\delta}{D} \quad \textbf{Equation 15}$$

where δ is the boundary thickness and D is the grain size.[11] C_1/C_o is equivalent to $(\delta/D)^2$ and $(\delta/D)^3$ for grain edges and corners, respectively.[11]

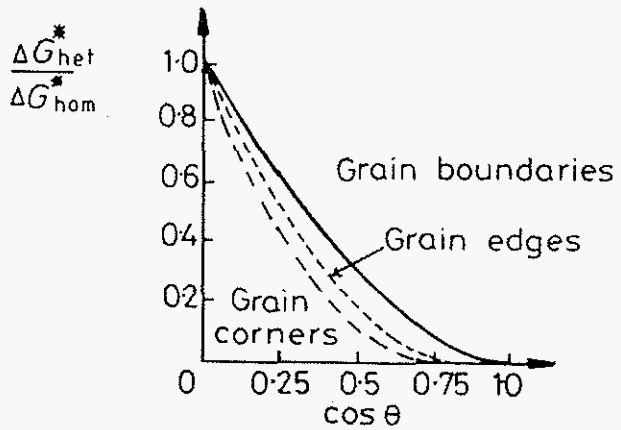

Figure 6 The effect of particle size on the activation energy of heterogeneous (grain boundary) nucleation compared to homogenous nucleation[11]

2.2.1.3 Precipitate Growth

After precipitates have nucleated, they start to grow. The growth rate of a precipitate depends on the rate of diffusion and the undercooling from the equilibrium temperature. Nucleation usually dominates precipitation at low undercoolings while growth dominates precipitation following the critical transformation rate temperature, as presented in Figure 7.

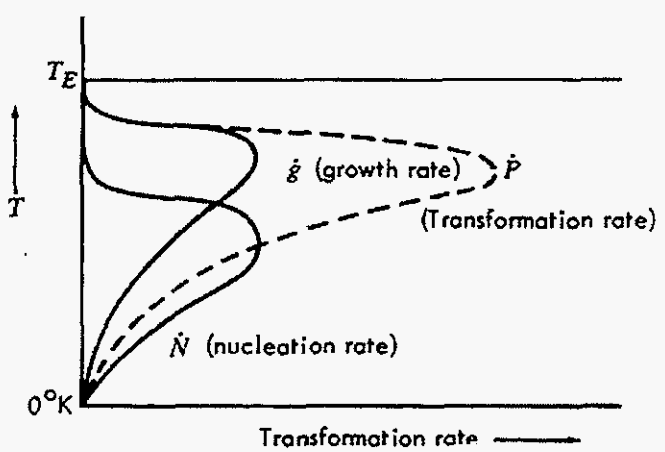

Figure 7 Transformation rate as a function of undercooling from the equilibrium temperature.[12]

As mentioned in the previous section of this chapter, precipitates will nucleate where the interface energy is at a minimum. The equilibrium precipitate morphologies are governed by the direction in which interfacial free energy is minimized. The direction of growth is governed by the type of interfaces between the precipitate and the neighboring phase. The precipitate usually has both immobile semi-coherent or coherent interfaces, and mobile incoherent interfaces (Figure 8). Disk- or plate-like morphologies usually form as a result.

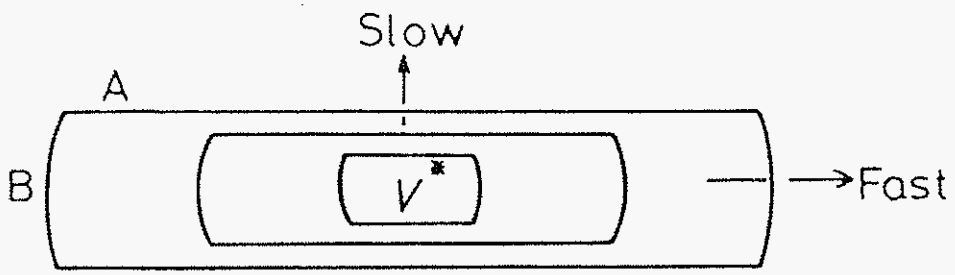

Figure 8 Influence of interference type on the mobility of the precipitate A) Semi-coherent interface B) Incoherent interface[11]

Grain boundary growth can occur in such a way that several planar incoherent interfaces may grow together to form a continuous line of precipitation. In this case, the grain boundary solute concentration would be much higher than in bulk, creating a depleted region in the matrix adjacent to the grain boundary. An example of diffusion controlled growth along a grain boundary is presented in Figure 9. Local equilibrium at the interface and diffusion controlled growth are assumed since the interface is incoherent.[11] The growth rate of the grain boundary precipitation is, therefore, a function of the concentration gradient, as discussed earlier in this chapter.

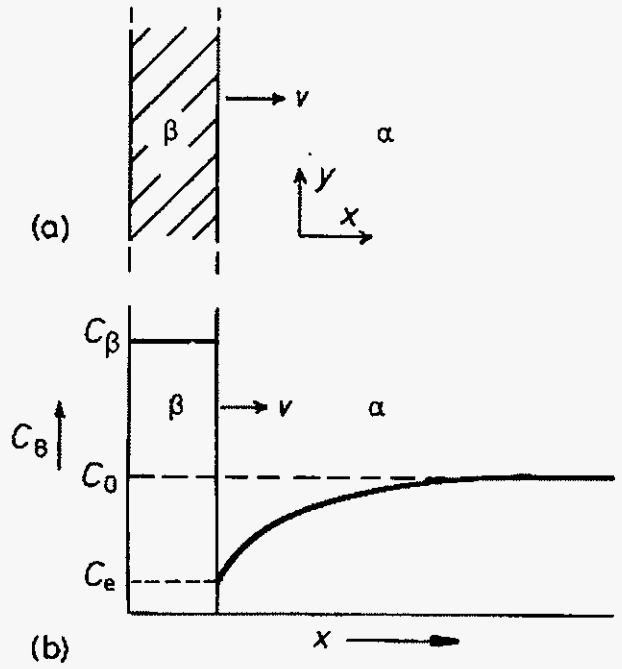

Figure 9 Diffusion-controlled growth at a grain boundary[11]

If the interface presented in Figure 9 has grown from zero width at a constant growth rate, v, there will be a concentration gradient at the interface, dC/dx. The concentration of the precipitate, matrix away from the grain boundary, and interface between the matrix and precipitate would be C_β, C_o, and C_e, respectively. For the interface to move a distance dx, the a volume must undergo a change where α containing C_e becomes β containing C_β, such that $(C_\beta - C_e)dx$ moles of B must be supplied by the diffusion through α. The flux of B for a length of time dt is given by D(dC/dx)dt, where D is the interdiffusion coefficient. If these equations are equaled then,

$$v = \frac{dx}{dt} = \frac{D}{C_\beta - C_e}\frac{dC}{dx} \qquad \textbf{Equation 16}$$

2.2.1.4 Precipitate Coarsening

A system is always unstable if the interfacial energy of the system is not at a minimum. A physical view would reveal that a high concentration of smaller precipitates would always coarsen into a low concentration of larger precipitates. If a situation exists similar to what is presented in Figure 9 with a spherical β precipitate surrounded by the α matrix, the kinetics of coarsening can be explained by the Gibbs-Thompson solubility relationship:

$$Cr = C_e\left(1-\frac{2\gamma V_m}{RTr}\right) \qquad \textbf{Equation 17}$$

where C_r is the composition of α in equilibrium with a β precipitate with radius r and V_m is the molar volume of the precipitate.

A concentration gradient will exist in the matrix between two precipitates with two different radii, as presented Figure 10a. The concentration of the matrix adjacent to a particle will increase as the radius decreases. This will cause diffusion to flow in the direction of the larger precipitate. Therefore, the larger precipitate grows at the expense of the smaller precipitate. Such a phenomenon is called the capillarity effect. The role of interfacial energy can be described by Figure 10b, where $r_\infty > r_1 > r_2$. As the radius increases, the interfacial energy will decrease and vice versa. As a result, the free energy per atom of precipitate is lower for larger particles. The outcome of this process is that the mean radius of a precipitate, $\bar{r}$, will increase with time. If the diffusion of the matrix is considered to be rate controlling, the diffusion controlled precipitate coarsening rate can be described by

$$\bar{r}^{3} - \bar{r}_o^{3} = \frac{3}{8} D_\alpha \frac{C_e^\alpha}{C_e^\beta - C_e^\alpha} \frac{2\gamma V_m}{RT} t \qquad \textbf{Equation 18}$$

where $\bar{r}_o$ is the mean radius at time t = 0. The rate of coarsening will also increase with temperature, although, at a slower rate than growth.

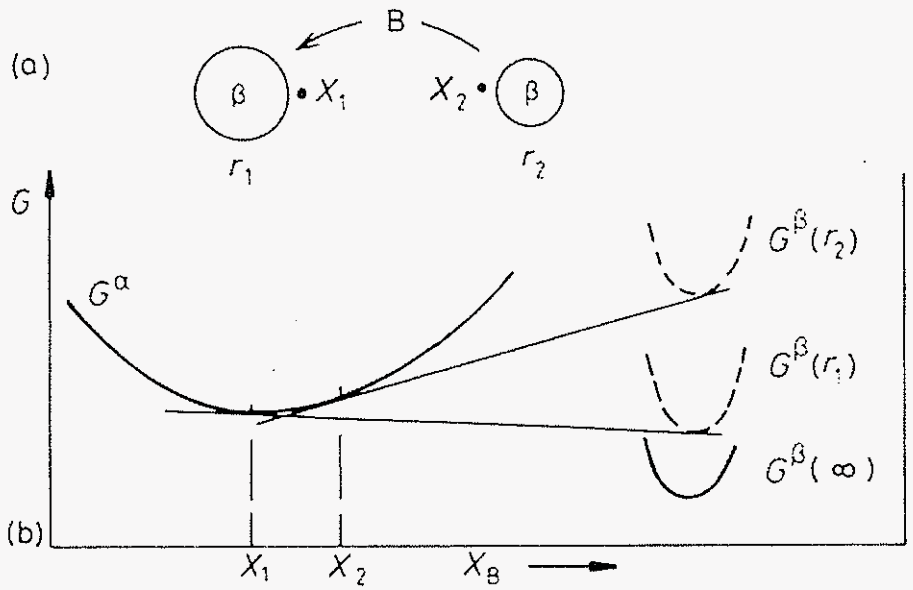

Figure 10 Coarsening as shown by the a) capillarity effect b) molar free energy as a function of concentration for precipitates with increasing radii[11]

2.2.2 Time-Temperature-Transformation (TTT) Diagrams

The combination of nucleation and growth is what determines the equilibrium conditions of a phase. Nucleation dominates the transformation at lower temperatures up to the critical transformation rate, growth governs the transformation up until equilibrium, and coarsening takes over after equilibrium has been reached. General trends for nucleation, growth, and coarsening are presented in Figure 11 by displaying volume percent and number density as a function of time. As a result, isothermal phase transformation diagrams can be determined that show the fraction transformed as a function of time and temperature, as presented in Figure 12. These diagrams are commonly C-shape, and referred to as time-temperature-transformation (TTT) diagrams or isothermal transformation (IT) diagrams. The

critical transformation rate, or minimum time for transformation to occur, is found at the nose of the C curve. TTT diagrams can also be used to represent material properties as a function time and temperature instead of isothermal transformation rates.[12]

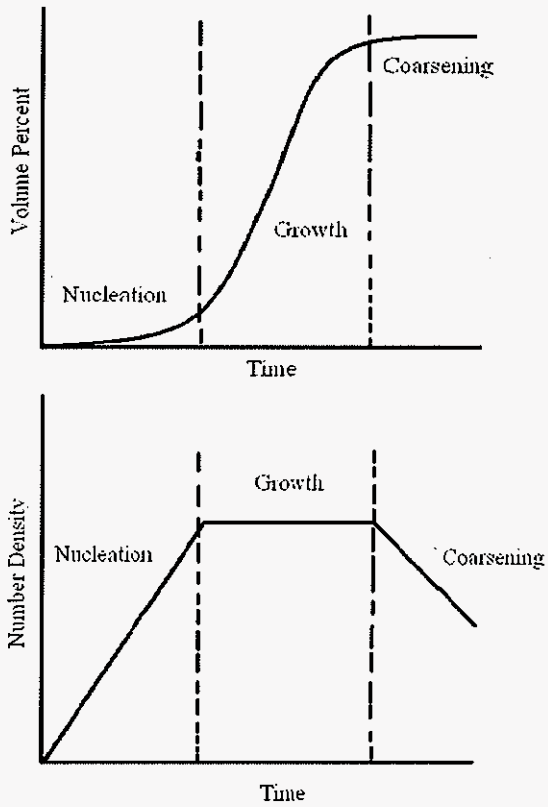

Figure 11 General nucleation, growth, and coarsening trends

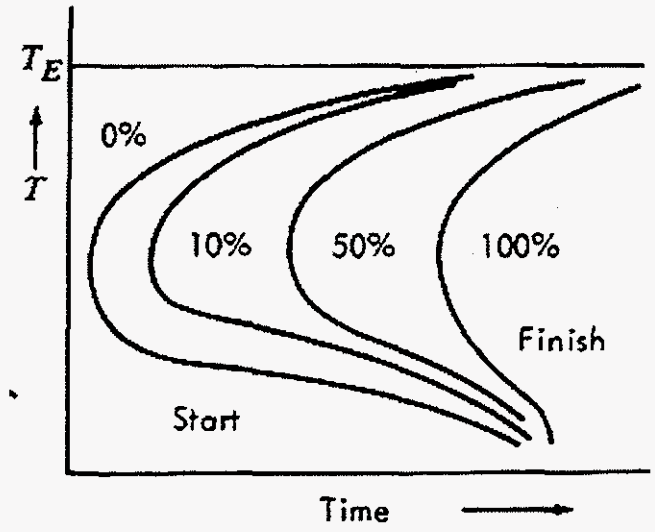

Figure 12 Example TTT curves[13]

The extent of phase formation as a function of isothermal hold time is described by the Johnson-Mehl-Avrami equation.[7] The simplest form of this equation can be written as:

$$f = 1 - \exp(-kt^n) \qquad \textbf{Equation 19}$$

where f is the fraction transformed, k is a temperature sensitive constant that depends on the nucleation and growth rates in min^{-1}, and n is a numerical exponent that is independent of temperature, provided there is no change in nucleation mechanism.[11] In order to determine the transformed volume percent (f) it is first necessary to determine the equilibrium volume percent (V_e) at the temperature of interest. The equilibrium volume percents can be determined in various ways depending on the growth rates, and will be described later. Typical n values are listed in Table IV for various phase transformation conditions.

TTT diagrams are completed by observing the desired change in properties or phase percentages following isothermal holds for a given amount of time followed by quenching. Samples are first heated to homogenizing temperature to ensure a common starting point and

then quenched down to a desired temperature where they are isothermally held for a desired amount of time. The samples are then quenched to room temperature and prepared for the desired characterization. The extents of transformation are obtained by first taking images of the microstructure and then phase percentages can be determined with the help of image analysis software. Experimentally determined phase percentages are then normalized to represent the fraction transformed, f. The Avrami Equation (Equation 19) is then used to calculate a series of curves, one for each temperature, which are used to determine the TTT diagrams, as is presented in Figure 13.

Table IV Typical n values under various phase transformation conditions[15]

a) Polymorphic changes, discontinuous precipitation, eutectoid reactions, interface controlled growth, etc.

Conditions	n
Increasing nucleation rate	>4
Constant nucleation rate	4
Decreasing nucleation rate	3-4
Zero nucleation rate (saturation of point sites)	3
Grain edge nucleation after saturation	2
Grain boundary nucleation after saturation	1

b) Diffusion controlled growth

Conditions	n
All shapes growing from small dimensions, increasing nucleation rate	>2.5
All shapes growing from small dimensions, constant nucleation rate	2.5
All shapes growing from small dimensions, decreasing nucleation rate	1.5-2.5
All shapes growing from small dimensions, zero nucleation rate	1.5
Growth of particles of appreciable initial volume	1-1.5
Needles and plates of finite long dimensions, small in comparison with their separation	1
Thickening of long cylinders (needles) (e. g. after complete end impingement)	1
Thickening of very large plates (e. g. after complete edge impingement)	0.5

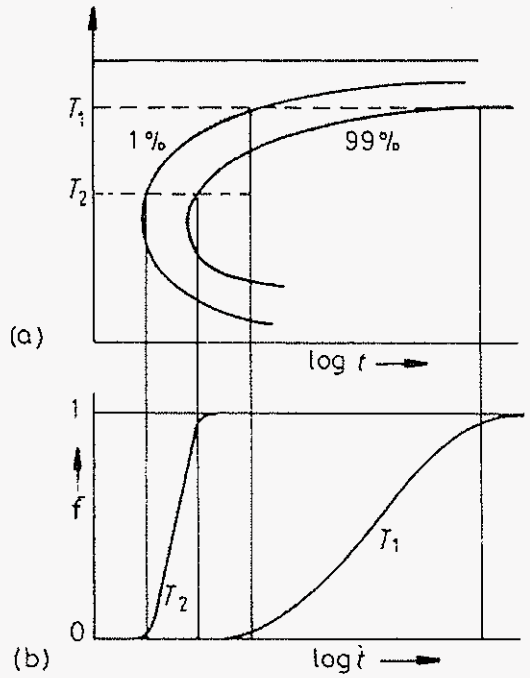

Figure 13 a) Example TTT diagram b) Corresponding Avrami curves[11]

2.3 Metallurgy and Properties of Cast Superaustenitic Stainless Steels

2.3.1 Designations of Superaustenitic Stainless Steels

Superaustenitic stainless steels CN3MN and CK3MCuN are designated by the Alloy Designation System (ACI). Cast Stainless steels are split into two categories: corrosion-resistant (C) and heat-resistant alloys (H). The first letter of the alloy designation refers to one of these categories. Corrosion resistant castings are used in aqueous environments up to 650°C. The second letter in the designation refers to the Ni and Cr content in the alloy. Figure 14 shows the amount of Ni and Cr that corresponds to each level. The number in the middle represents the amount of carbon in the alloy times 100 percent. Other letters that follow refer to major alloying elements, such as M for molybdenum. CN3MN refers to an alloy that is

corrosion-resistant, of the 20Cr-25Ni type, has a maximum of 0.03% C and has major alloying elements Mo and N. CK3MCuN refers to an alloy that is corrosion-resistant, of the 25Cr-20Ni type, has a maximum of 0.03% C and has major alloying elements Mo, Cu and N.

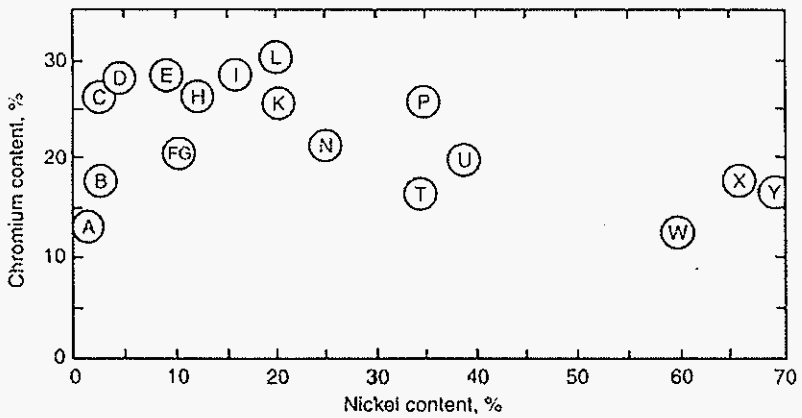

Figure 14 Ranges of Cr and Ni in cast stainless steel alloys as designated by the ACI system[7]

Due to the high amount of wrought production, in tonnage, cast versions of wrought grades are commonly available.[7] Wrought and cast alloys are produced differently, and as a result have different microstructures. Wrought material requires the ability to be hot- and cold-worked, while cast alloys must maintain high fluidity when poured. This is why high Si levels are often found in cast alloys. The mechanical properties may also be different, as the grains in cast alloys are generally larger while the grains in wrought alloys are more directional. Table V lists the wrought counterparts of CN3MN and CK3MCuN and other designations used to identify these alloys.

Table V Wrought equivalents and other designations of CN3MN and CK3MCuN[7]

ACI Standard	Wrought Counterparts	Designations	
		ASTM	UNS
CN3MN	AL-6XN	A 743, A744	J94651
CK3MCuN	2545MO	A 351, A 743, A744	J93254

2.3.2 Microstructures

Superaustenitic stainless steels are compositional balanced with Ni to ensure a purely γ matrix. When superaustenitic stainless alloys are exposed to elevated temperatures, intermetallic precipitates and carbides often form. The most commonly observed secondary phases include $M_{23}C_6$ carbide, and intermetallic sigma, chi, and Laves phases.[1-5] Other less common secondary phases found in some superaustenitic alloys include M_6C, π, R and Cr_2N.[1-5] High amounts of these phases reduce the corrosion resistance and mechanical properties of the stainless steel.

The type of precipitate strongly depends on the local composition and heating time and temperature. At temperatures ranging from 700-1100°C, carbides are usually the first to form.[1] At longer times, these carbides are usually replaced by intermetallic compounds, such as σ, χ, and Laves.[1] Low carbon solubility has been found in σ, while a high solubility of interstitial elements in the austenite matrix tends to favor the formation of χ and Laves phases.[1] Increased Mo percentages favor the precipitation of intermetallics at higher temperatures. High amounts of N (0.5 wt %) have been found to prevent the χ phase from forming at all; rather, the formation of the Laves phase is reported.[1,3] However, the Laves phase formation is delayed with additional N.[1] Thus, the addition of N not only increases the mechanical properties of these materials, but also proves useful in delaying, or even preventing, harmful precipitates from ever forming.

2.3.3. TTT Diagrams of Superaustenitic Stainless Steels

There have only been a few studies done on the transformation of superaustenitic stainless steels, and all of them were done on wrought alloys. Transformations of wrought alloy 254 SMO and 654 SMO were studied by Svoboda et al.[3]. It was reported that the σ,

Laves, and π phases were present at 700°C up to 6170 hours. The study used the thermodynamic Calphad[16] method to calculate phase equilibrium coupled with growth kinetics modeling software, JmatPro, to calculate TTT diagrams for 5% transformation of σ-, χ- and Laves-phases for 654 SMO (Fe-24.4Cr-22Ni-7.3Mo-3.65Mn-0.5N), as presented in Figure 15.[3] A nucleation mechanism was neglected in this case. Kovach et al.[8] also reported on the 254 SMO alloy (Fe-19.9Cr-17.6Ni-6.1Mo-0.5Mn-0.2N) and a TTT diagram on the total precipitation along the grain boundaries from this experiment is presented in Figure 16. Details concerning the rate of transformations or type of precipitation were not mentioned.

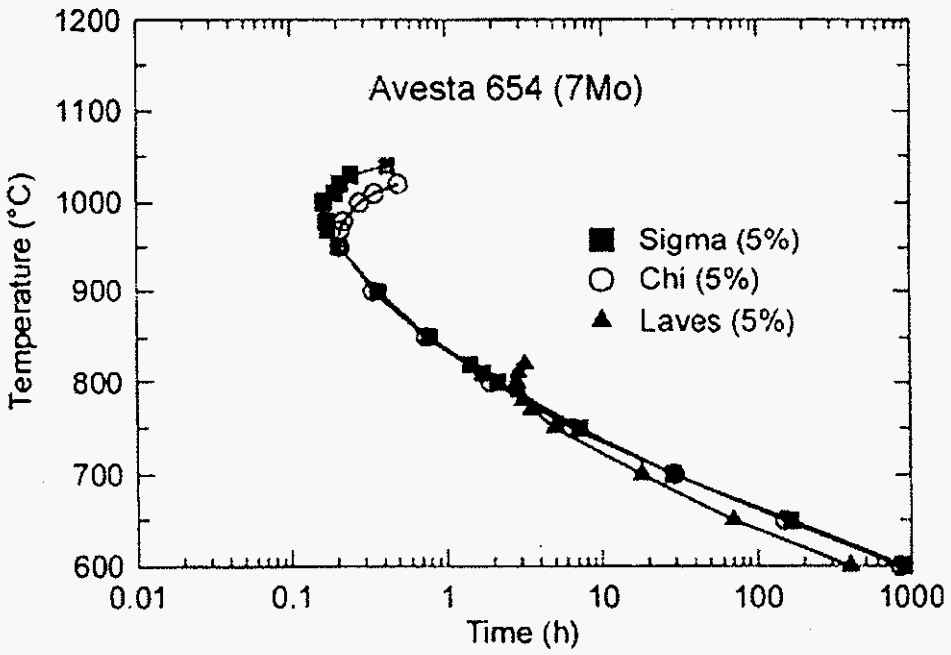

Figure 15 TTT diagram as calculated by JmatPro software for sigma-, chi- and Laves-phases in wrought alloy 654 SMO[3]

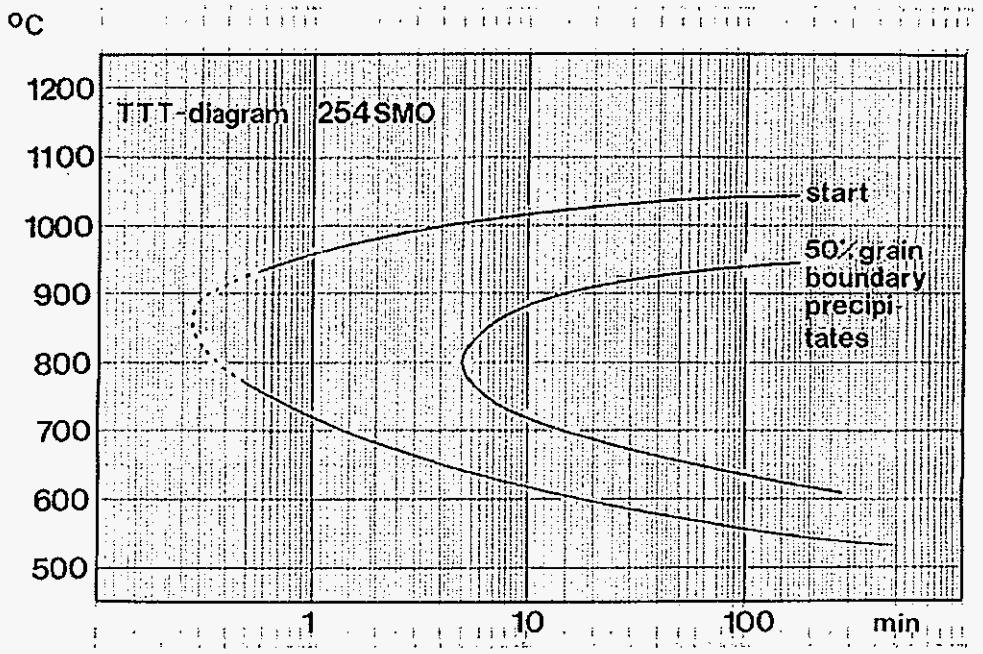

Figure 16 TTT diagram for grain boundary precipitation in wrought alloy 254 SMO[8]

CHAPTER 3: PROJECT AIMS

This study seeks to determine the isothermal transformation kinetics for cast superaustenitic stainless steel alloys CK3MCuN and CN3MN. This analysis depends on extensive heat treatments followed by a complete characterization of the samples with optical microscopy and backscattered and transmission electron microscopies. The transformation behavior will be further analyzed by determining volume percents and number densities of intermetallic phases as a function of heat treatment time and temperature. These analyses will be used to aid the understanding of the times and temperatures required for various phase transformations and equilibrium conditions. There has been a large amount of research on the mechanical and corrosion resistant properties of superaustenitic stainless steels. However, little work has been done on determining the transformation kinetics of the matrix to secondary phases as a function of time and temperature, and what has been done relates predominantly to wrought alloys. The results generated from this study will serve as a means to understand and control the role of various phase transformations during the production of superaustenitic stainless steel castings.

CHAPTER 4: EXPERIMENTAL PROCEDURE

Two heats each of CN3MN and CK3MCuN in the form of 3 x 4 x 35cm keel bars were received for examination in the solution heat treated condition, with the heat treatment being between 1160 and 1230°C (2125 and 2250°F) for at least 2 hours. A list of the compositions as determined by the foundry is presented in Table VI. For short term treatments slices from each bar were suspended by a wire in a vertical furnace before being dropped into a salt bath. For longer-term heat treatments, samples were encapsulated in quartz under an argon atmosphere, and placed in a box furnace.

Table VI Compositions as determined by the foundry for CN3MN and CK3MCuN keel bars

	CN3MN	CK3MCuN
C	0.023	0.025
Si	0.74	0.90
Mn	0.59	0.73
P	0.013	0.015
S	0.004	0.007
Cr	20.9	20.2
Mo	6.5	6.6
Ni	24.6	17.7
Cu	0.12	0.53
N	0.22	0.20

Samples were heat treated between 700 and 900°C from 1 minute to 2040 hours. Short-term heat treatments (up to 500 hours) were performed by transferring the sample directly from the vertical tube furnace to a salt bath. Longer heat treatments were performed in box furnaces. A matrix of the completed heat treatments is presented in Table VII.

Table VII Heat treatment matrix

	700°C	750°C	800°C	850°C	900°C
1 m	x	x	x	x	x
10 m	x	x	x	x	x
30 m	x	x	x	x	x
1 hr	x	x	x	x	x
10 hr	x	x	x	x	x
100 hr	x	x	x	x	x
500 hr	x	x	x	x	x
1000 hr	x		x		x
1500 hr	x		x		x
2040 hr	x		x		x

The samples for characterization were prepared using standard metallographic techniques. The center region of the samples was examined to avoid any surface effects. The transformation kinetics and resulting phases were analyzed with optical microscopy, scanning electron microscopy (SEM), and energy and wave-dispersive spectroscopy (EDS, WDS). More definitive characterization was carried out with transmission electron microscopy (TEM). TEM samples were prepared using a jet polisher. The solution used was 5% perchloric acid in 25% glycerol and 70% ethanol at -20°C and a potential of 50 volts. An energy dispersive spectrometer, which is attached to the TEM, was used as an initial screening of possible phases.

Several backscattered SEM or optical cross sections of each heat treatment were taken from randomly selected areas and an image analysis software program was used to determine the phase percentages for each cross section. It was assumed that the area fraction was equal to the volume fraction. The resulting volume fractions for each phase were

averaged. Number densities were also calculated from the same cross sections as the number of particles per cm^2. These values are also assumed to represent volume densities. TEM was used as a definitive characterization of the phases in both alloys. Diffraction patterns of the phases were generated and analyzed to determine crystal structure and lattice parameters. The crystal structure and lattice parameters were then compared to literature data of phases typically found in stainless steels (Table VIII). The formation temperatures of the secondary precipitates found in Table VIII were not given; however, it is assumed that the lattice parameters are similar at all formation temperatures.

Table VIII Typical phases and crystallographic properties found in superaustenitic stainless steels[2]

Phases	Lattice Type	Space Group	Lattice Parameter, Å	Composition, wt%
σ	BCT	$P4_2/mnm$	a=8.80, c=4.54	35Fe-40Cr-12Ni-14Mo
χ	Cubic	$I\bar{4}3m$	a=8.92	34.5Fe-34.2Cr-9.3Ni-22.0Mo
M_6C	FCC	Fd3m	a=10.95	14Fe-18.8Cr-12.7Ni-51.2Mo
R	Trigonal	$R\bar{3}$	a=10.903, c=19.342	25Fe-20Cr-6.4Ni-45Mo
Laves	HCP	$6_3/mmc$	a=4.744, c=7.725	38Fe-11Cr-6Ni-45Mo
π	Cubic	$P4_132$	a=6.36	19Fe-47Cr-20Ni-13Mo
Cr_2N	HCP	$P\bar{3}1m$	a=4.80, c=4.47	3Fe-83Cr-3Ni-9Mo

CHAPTER 5: EXPERIMENTAL RESULTS

5.1 CK3MCuN

5.1.1. Phase Characterization

Contrast variations in backscattered electron (BSE) images made it possible to differentiate between phases due to atomic number differences. Precipitation of intermetallic phases was found after heat treatments at low temperatures (700°C) and short soak times (1 minute) in CK3MCuN. Figure 17 shows examples of typical microstructures observed after long aging times. While precipitation starts along the interdendritic boundaries, growth continued both at the boundaries and homogeneously within the dendrites as heat treatment times and temperatures increased. A coarsened gray phase is first seen along the interdendritic boundaries; shortly thereafter a needle-like white phase precipitates. Further analysis of the microstructures seen at various times and temperatures will be presented in section 5.1.2.

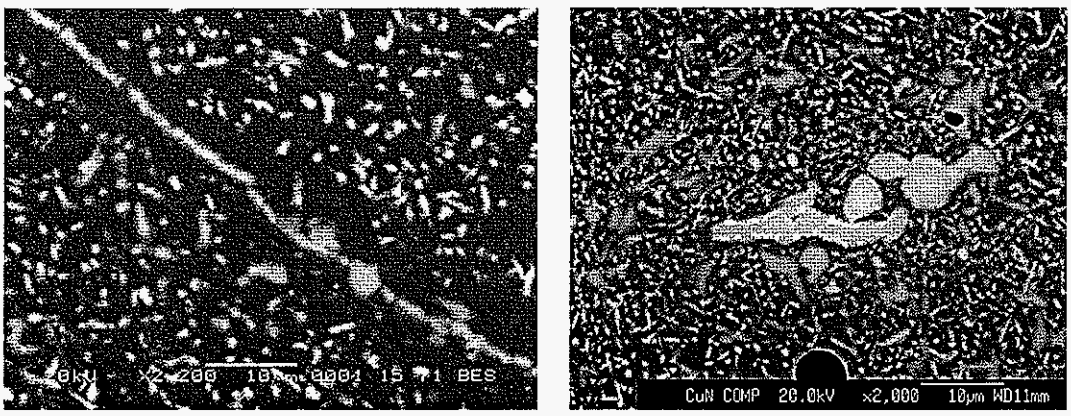

Figure 17 Backscattered images of CK3MCuN after 850 °C for 500 hours (left) and 800 °C for 500 hours (right)

Results obtained from WDS scans of several white and gray precipitates seen in the 900°C, 500 hour heat treatment sample are presented in Table IX. These quantitative compositions were used as a comparison to the qualitative EDS compositions, which were determined as an initial screening of phases to be identified with TEM. For the TEM phase identification, a CK3MCuN sample heat treated at 800°C for 500 hours was used, since the largest concentrations of both precipitates were observed for this time and temperature. After an area was found where each precipitate was identified, a combination of selected area diffraction (SAD) and convergent beam electron diffraction (CBED) was used. The diffraction results were compared to crystallographic information found in Table IX.

Table IX Microprobe WDS results for CK3MCuN after 500 hours at 900 °C

Composition (wt. %)						
Si	**Fe**	**Mo**	**Cr**	**Ni**	**Mn**	**Phase**
2.6	40.7	28.0	17.2	10.5	0.5	White
1.4	42.6	12.8	31.9	9.7	0.6	Gray
0.9	57.0	2.2	22.2	16.9	0.8	Matrix

The most commonly observed precipitate in CK3MCuN samples was the high-Cr σ phase. An example of a σ precipitate, along with a SAD pattern from a [001] zone axis, is presented in Figure 18. The σ phase has a body centered tetragonal crystal structure where a=4.57Å and c=8.76 Å. The high-Mo Laves phase was also observed in regions where σ was found. An example of a Laves precipitate, along with a SAD pattern from a $[2\bar{1}\bar{1}0]$ zone axis, is presented in Figure 19. The Laves phase has hexagonal crystal structure where a=4.74 Å

and c =7.70 Å. A comparison of the experimental and literature lattice parameters is presented in Table X.

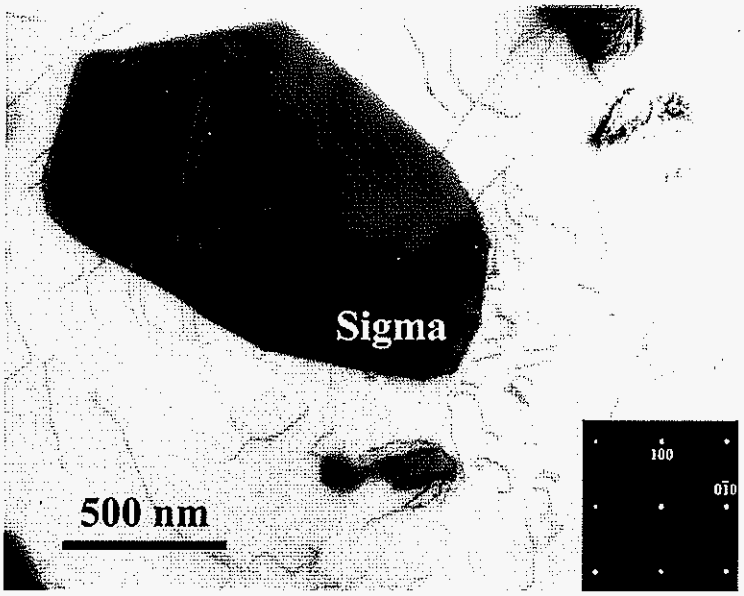

Figure 18 Bright field image of σ phase and corresponding SAD pattern with a [001] zone axis in a CK3MCuN sample heat treated at 800°C for 500 hours

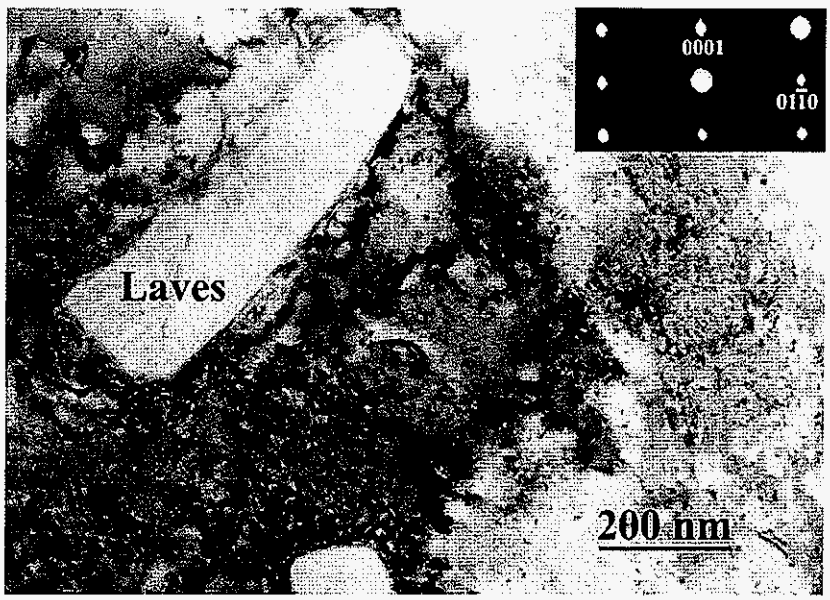

Figure 19 Bright field image of Laves phase and corresponding SAD pattern with a [2 $\bar{1}\bar{1}$ 0] zone axis in a CK3MCuN sample heat treated at 800°C for 500 hours

Table X Experimental and literature lattice parameters for σ and Laves in CK3MCuN

Phases	Lattice Type	Experimental Lattice Parameter, Å	Literature Lattice Parameter[2], Å	EDS Composition, wt%
σ	BCT	a=8.76, c=4.57	a=8.80, c=4.54	23.6Fe-45.7Cr-16.3Ni-12.6Mo
Laves	HCP	a=4.74, c=7.70	a=4.744, c=7.725	25.4Fe-11.5Cr-7.4Ni-52.6Mo

5.1.2. Phase Transformation Behavior

Both σ and Laves contain Fe, Cr, Mo, Ni, and Si. The Laves phase is rich with Mo, which causes it to appear brighter than the Cr-high σ phase in BSE images. Metallographic examination of CK3MCuN samples showed a small amount of σ phase was present in the solution heat treated samples before the isothermal hold. Nucleation of the σ phase was low until approximately 100 hours at all temperatures, after which an increase in the number of precipitates was seen. Subsequent growth occurred very slowly, such that equilibrium was not reached at 700 and 800°C even after the maximum heat treatment time of 2040 hours. Volume percents seen after this time are above 20%. The amount of σ at 900°C leveled off at ~12%. Measured σ volume percentage data with error bars of one standard deviation are presented with a best-fit curve in Figure 20.

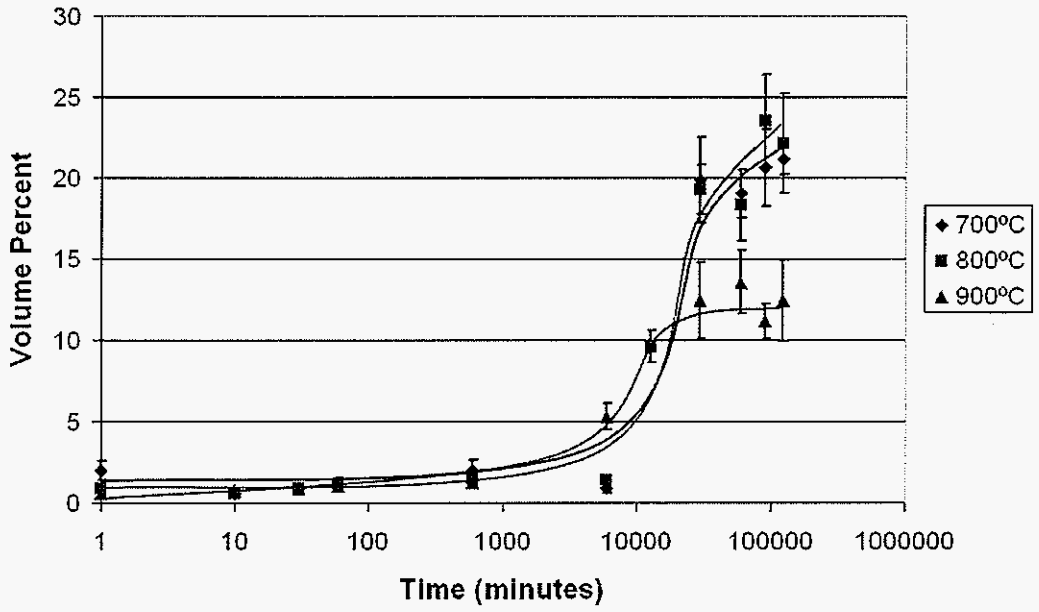

Figure 20 Experimental σ volume percents and best fit curve for CK3MCuN

Metallographic examination did not reveal any Laves present in the solution heat treated structure. However, Laves was present after about 30 minutes at 900°C and 500 hours at 700 and 800°C. The Laves phase reached a maximum of 4.6, 6.8, and 10.0% at 700, 800, and 900°C, respectively, at 500 hours. The dissolution of Laves phase was apparent after 100, 250, and 500 hours at 900, 800, and 700°C, respectively. Measured Laves volume percentage data with error bars of one standard deviation are presented with best-fit curves in Figure 21.

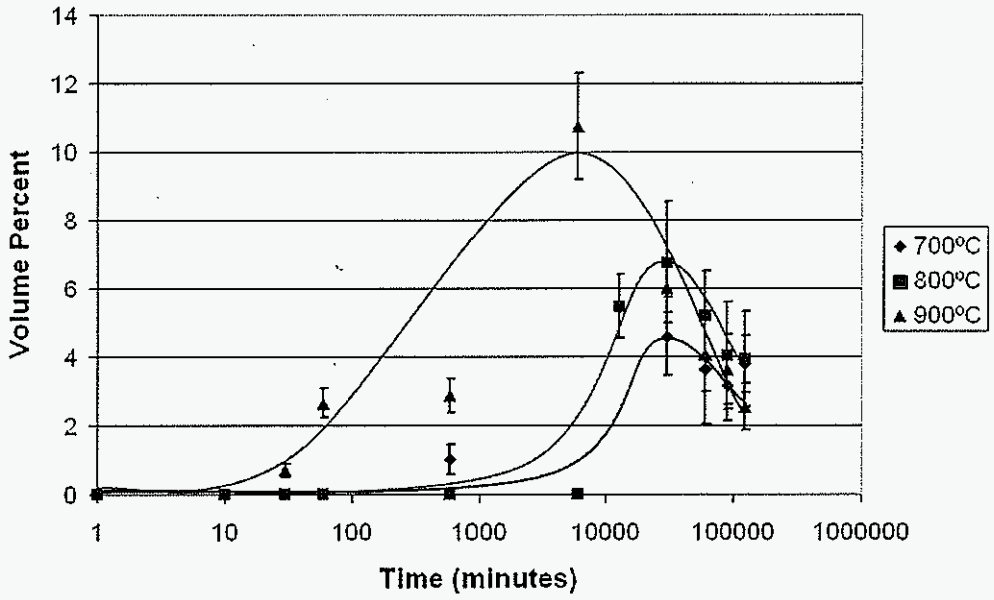

Figure 21 Experimental Laves volume percents in CK3MCuN and best fit curve

The results presented in Figures 20 and 21 were compared with equilibrium volume percents as calculated by the thermodynamic software program *Thermo-Calc*. *Thermo-Calc* uses appropriate thermodynamic databases to determine such things as driving force and equilibrium phase percentages and compositions. The nominal compositions, as seen in Table VI, were used to determine equilibrium phases and volume percents between 700 and 900°C for CK3MCuN. As presented in Figure 22, *Thermo-Calc* did not predict any Laves formation at equilibrium. Instead, a high amount of chi was predicted between 700 and 900 °C. A high amount of ferrite was predicted at 700°C with no austenite being predicted at equilibrium at any temperature. This was clearly an error since the matrix is known to be 100% austenite at all temperatures for superaustenitics. Comparison for 700 and 800°C cannot be made as experimental volume percents have not reached equilibrium conditions; however, the amount of σ predicted at 900°C where equilibrium appears to have been

reached is much higher than what is seen experimentally. Thus, present databases appear to be highly inaccurate for superaustenitic stainless steels, preventing *Thermo-Calc* from being used to determine equilibrium volume percents.

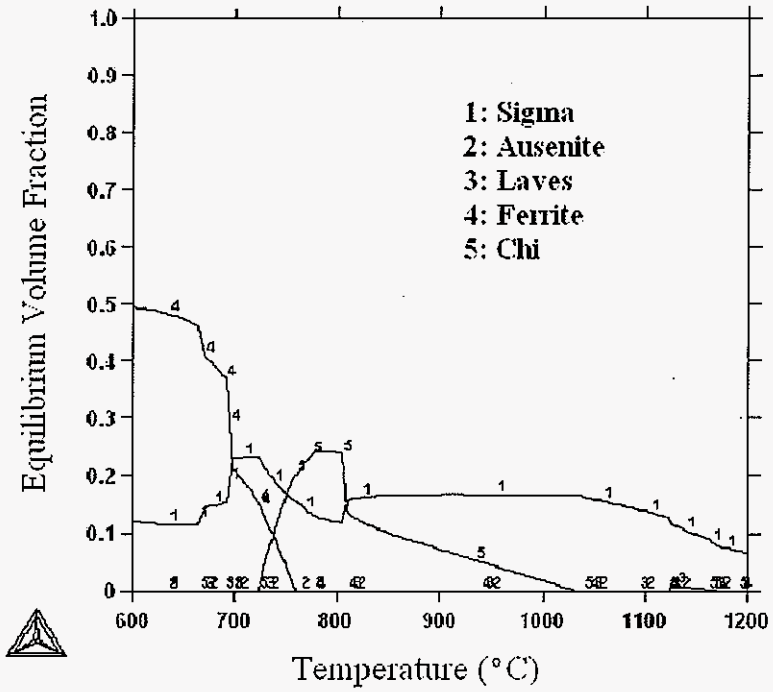

Figure 22 Equilibrium phases and volume fractions as calculated with *Thermo-Cal* for CK3MCuN

The contrast of phases in the BSE images also made it possible to calculate the number densities of σ and Laves for all heat treatments. The volume percentages are compared to the number densities for σ and Laves at 700, 800, and 900°C in Figures 23, 25, and 27, respectively. Number densities were measured as the number of precipitates per $0.01mm^2$ and are graphed with one standard deviation error bars. Microstructures that correspond to these models are presented in Figures 24, 26, and 28. Both σ and Laves precipitates found along the interdendritic boundaries and near voids were much larger than

precipitates found within the dendrites. Also, the average precipitate sizes are displayed larger than the actual sizes where only interdendritic boundary nucleation is present since the image analysis software counted an interdendritic boundary as one continuous precipitate.

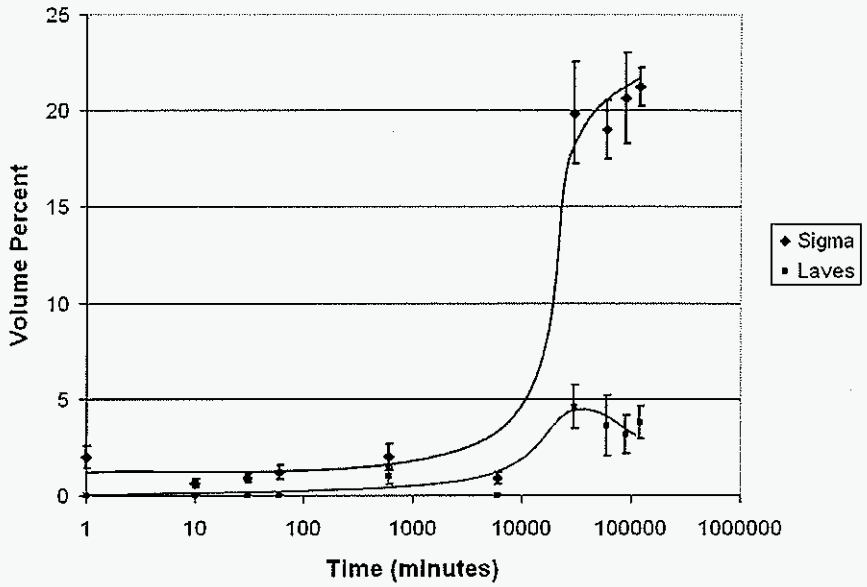

a)

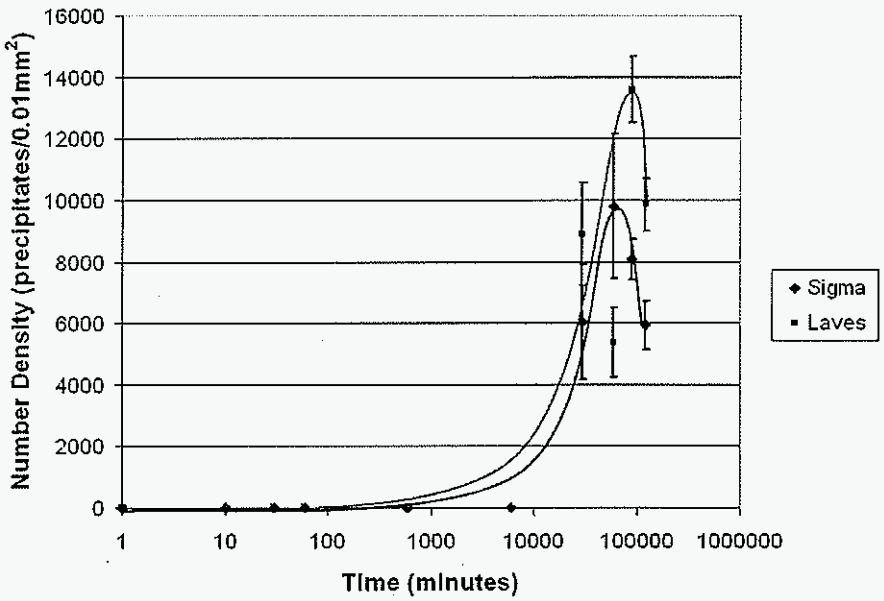

b)

Figure 23 Volume percents (a) and number densities (b) of σ and Laves at 700°C in CK3MCuN

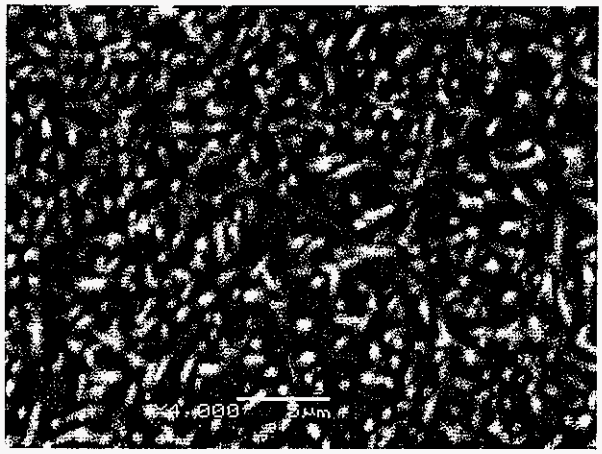

(a)

Average particle size of σ: 0.19μm^2 Laves: 0.05μm^2

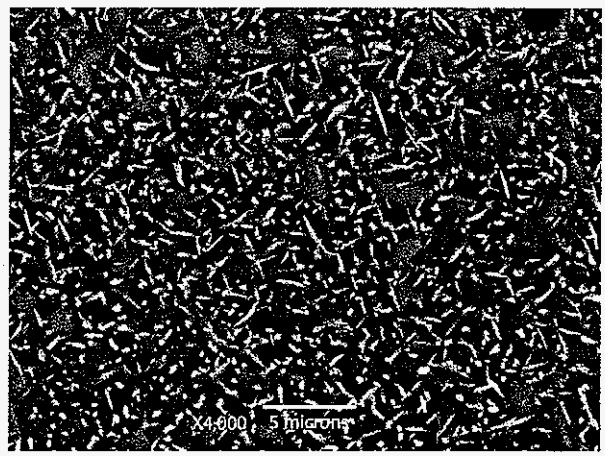

(b)

Average particle size of σ: 2.5μm^2 Laves: 0.06μm^2

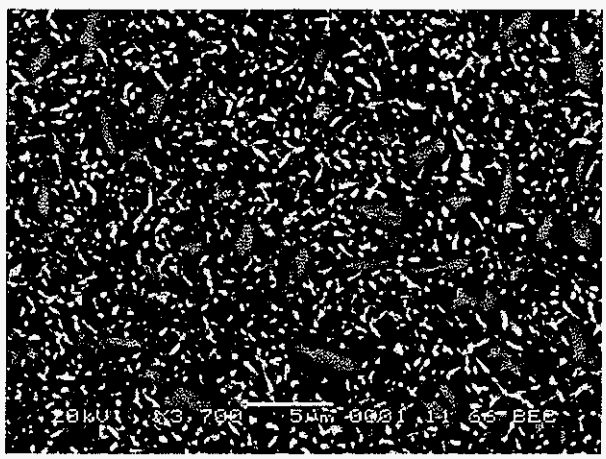

(c)

Average particle size of σ: 2.8μm^2 Laves: 0.04μm^2

Figure 24 BSE images of CK3MCuN at 700°C for (a) 1000 hours (b)1500 hours (c) 2040 hours

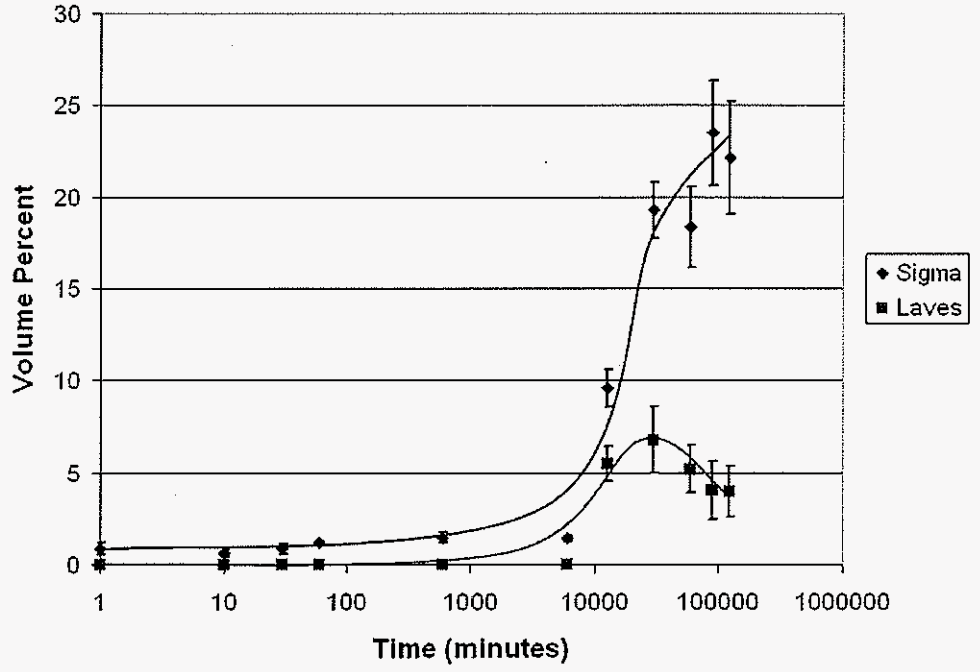

a)

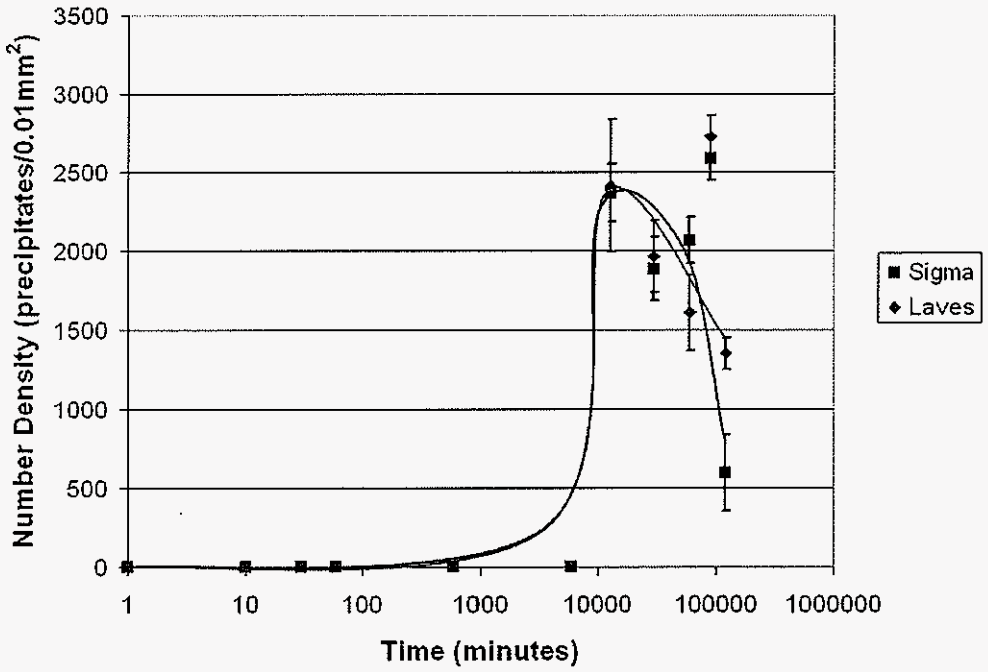

b)

Figure 25 Volume percents (a) and number densities (b) of σ and Laves at 800°C in CK3MCuN

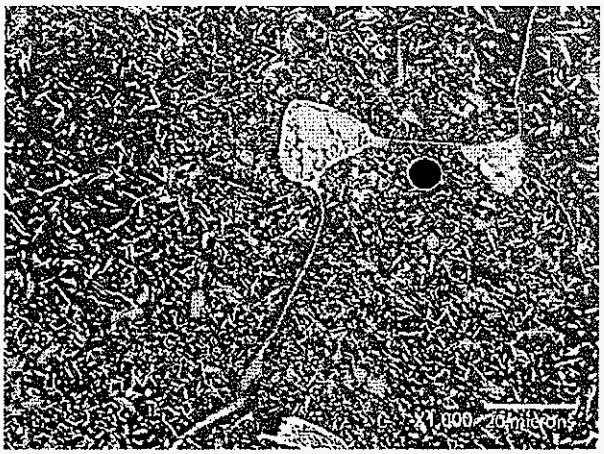

(a)

Average particle size of σ: 1.02μm^2 Laves: 0.34μm^2

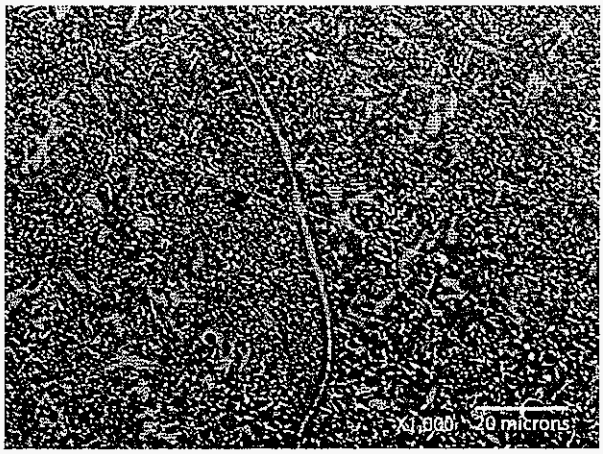

(b)

Average particle size of σ: 0.90μm^2 Laves: 0.15μm^2

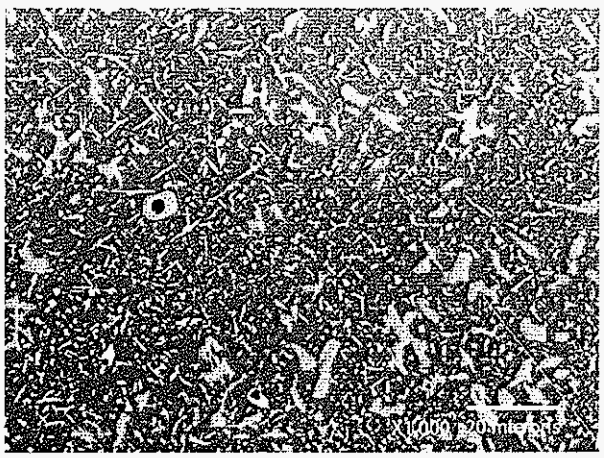

(c)

Average particle size of σ: 0.72μm^2 Laves: 0.29μm^2

Figure 26 BSE images of CK3MCuN at 800°C for (a) 500 hours (b) 1500 hours (c) 2040 hours

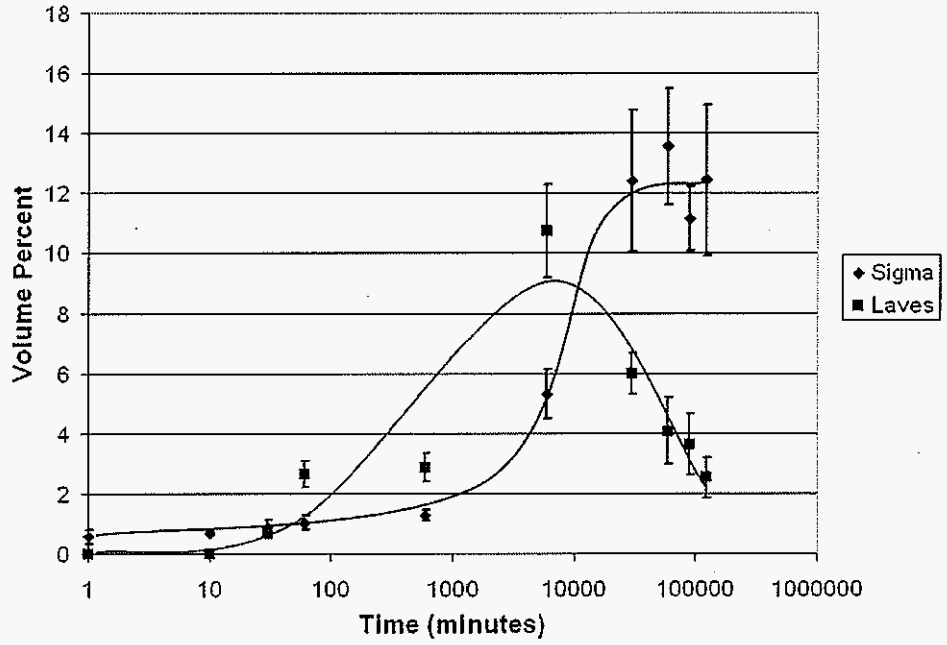

a)

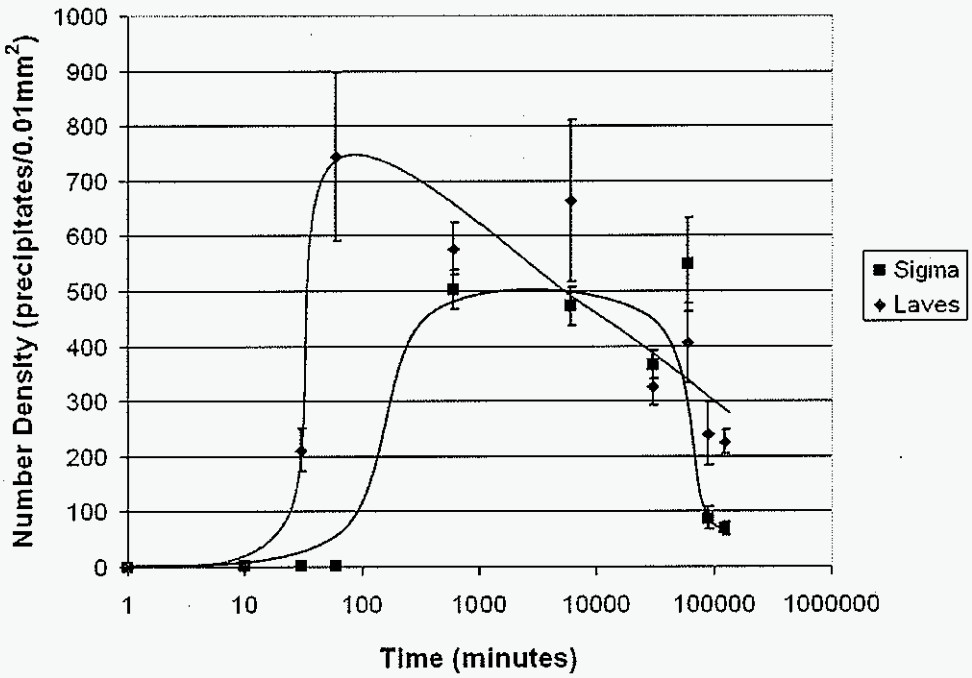

b)

Figure 27 Volume percents (a) and number densities (b) of σ and Laves at 900°C in CK3MCuN

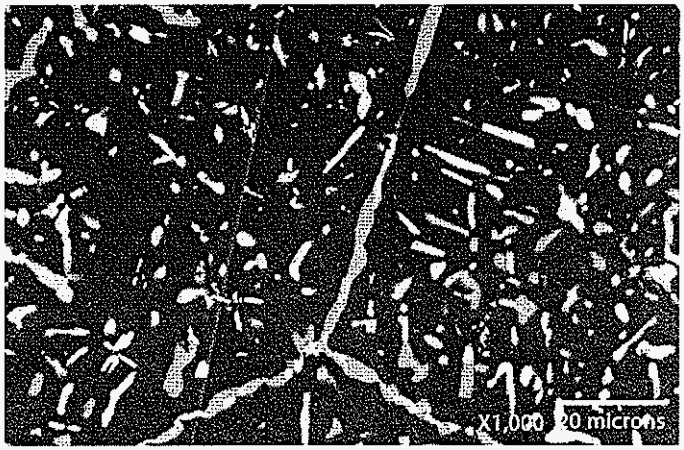

(a)

Average particle size of σ: 2.39μm^2 Laves: 1.84μm^2

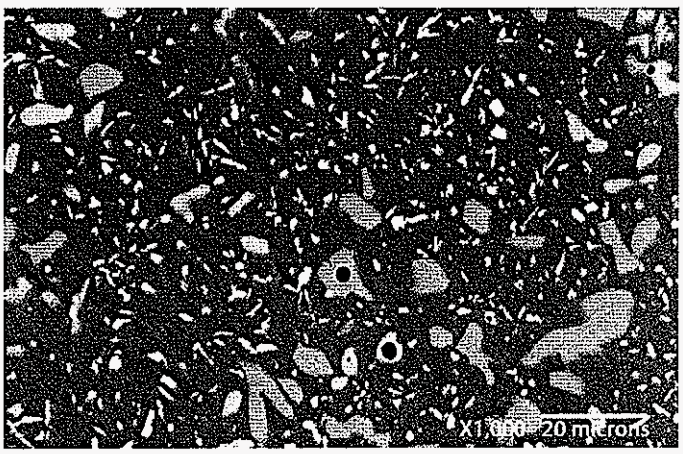

(b)

Average particle size of σ: 2.48μm^2 Laves: 1.01μm^2

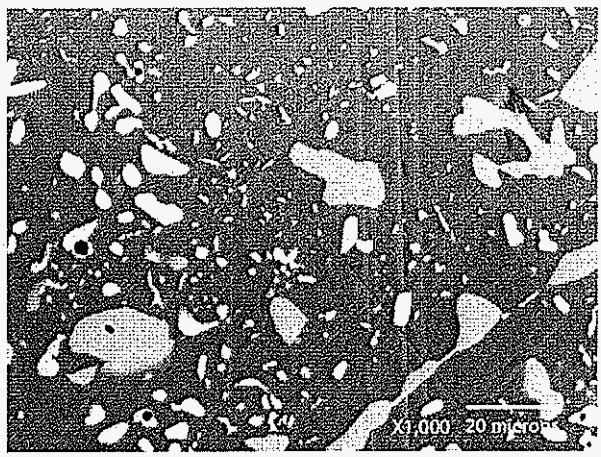

(c)

Average particle size of σ: 18.1μm^2 Laves: 1.12μm^2

Figure 28 BSE images of CK3MCuN at 900°C for (a) 500 hours (b)1000 hours (c) 2040 hours

5.2 CN3MN

5.2.1. Phase Characterization

Intermetallic phases similar to what were seen in CK3MCuN were observed at similar temperatures in CN3MN. Precipitation again was observed to first form along the interdendritic boundaries, although the scale of the precipitates was much finer than that of CK3MCuN for aging times up to 500 hours. Phase characterization proved to be extremely difficult in this alloy due to the fine scale of the precipitates, which was below the spatial resolution of EDS and WDS using SEM techniques for accurate chemical analysis. TEM was used again to positively identify the phases in CN3MN. Both σ and Laves were found in a sample heat treated at 800°C for 2040 hours. An example of a σ precipitate, along with a SAD pattern from a [100] zone axis, is presented in Figure 29. The high-Mo Laves phase was also observed with diffraction in the same heat treatment, but in a different sample due to macrosegregation effects that will be described later in this section. An example of a Laves precipitate, along with a SAD pattern from a $[2\bar{1}\bar{1}0]$ zone axis, is presented in Figure 30. The lattice parameters and EDS compositions of both phases were very similar to those found for σ and Laves in CK3MCuN (Table X).

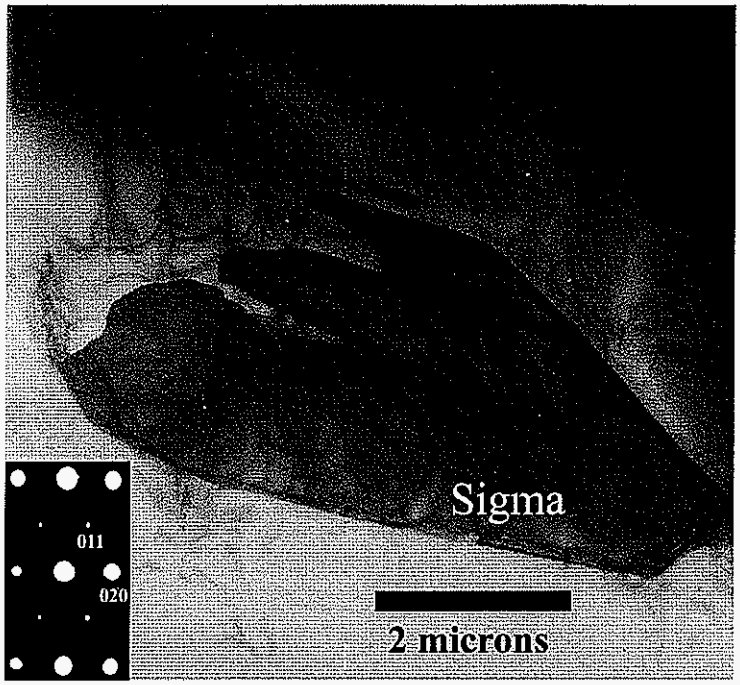

Figure 29 Bright field image of σ phase and corresponding SAD pattern with a [100] zone axis in a CN3MN sample heat treated at 800°C for 2040 hours

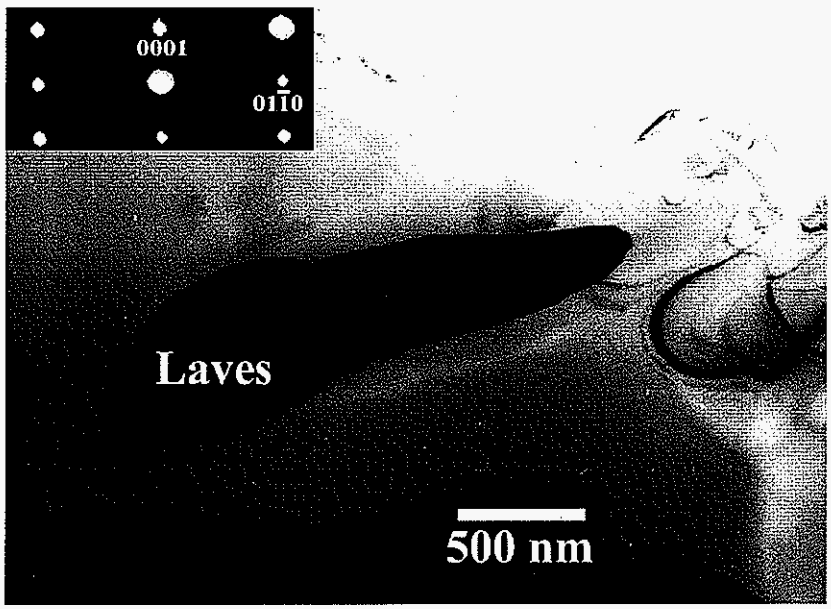

Figure 30 Bright field image of Laves phase and corresponding SAD pattern with a [2 $\bar{1}\bar{1}$ 0] zone axis in a CN3MN sample heat treated at 800°C for 2040 hours

Differentiation between σ and Laves based on contrast using backscattered electrons was more uncertain for samples aged at shorter times since small Laves precipitates that might normally appear white due to atomic number contrast (i.e. Z contrast) could appear gray due to beam spreading effects. As the aging time increased the difference in contrast between phases became much more apparent, and appeared similar to what was found in CK3MCuN, as presented in Figure 31.

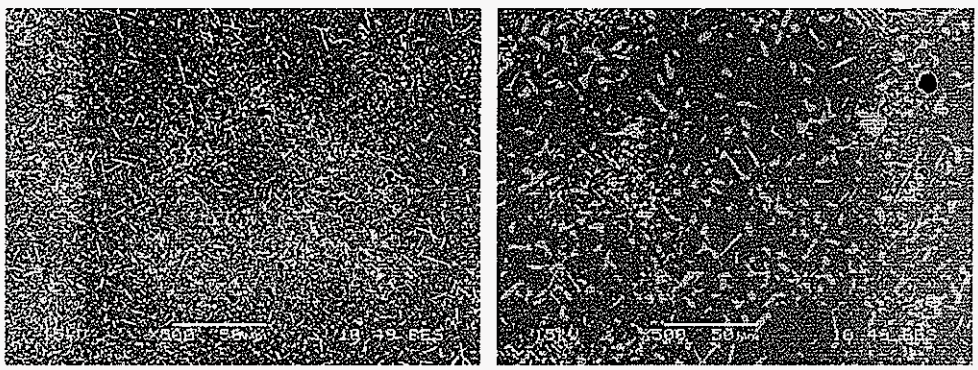

Figure 31 Backscattered images of 800 °C for 1000 hours (left) and 900 °C for 1000 hours (right)

Unlike CK3MCuN, a significant amount of macrosegregation corresponding to the original cast dendritic structure was observed at all temperatures for all times (Figure 32). At the longest times studied it was evident that growth of σ was favored in the former intradendritic regions while Laves was favored in the interdendritic regions. Compositional map scans using WDS revealed the macrosegregation of Mo in the solution heat treated samples as seen in Figure 33. The interdendritic region (high Mo concentration) would be favorable for Laves nucleation, while the intradendritic region (low Mo concentration) would be favorable for σ nucleation.

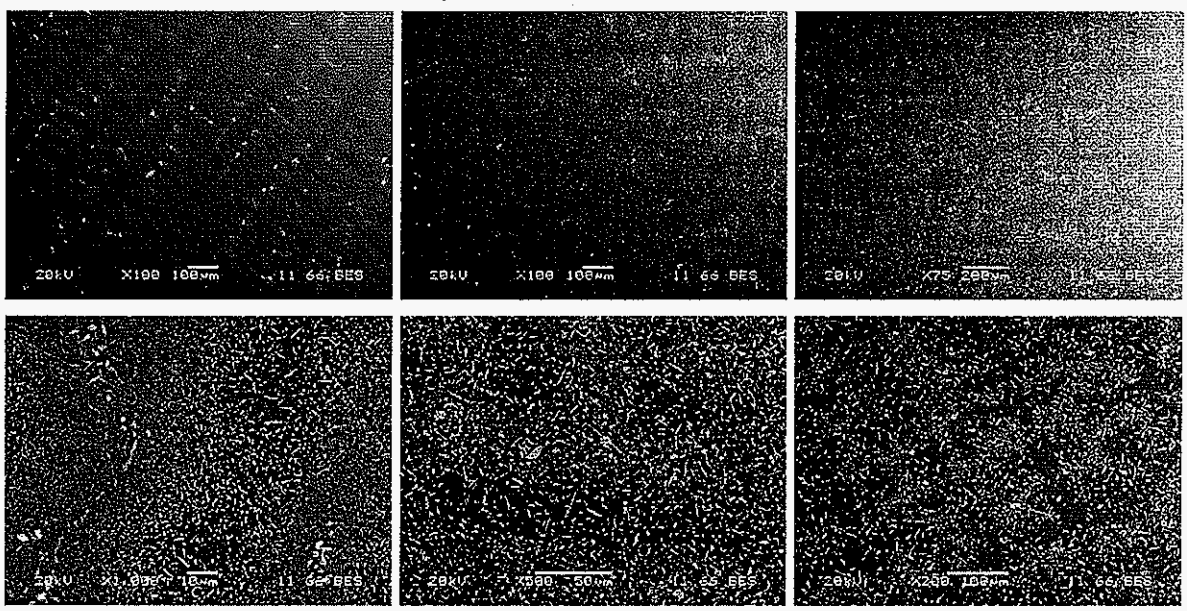

Figure 32 Backscattered SEM images taken at low magnification (top) and high magnification (bottoms) after 2040 hours at 700 °C (left), 800 °C (middle), and 900 °C (right)

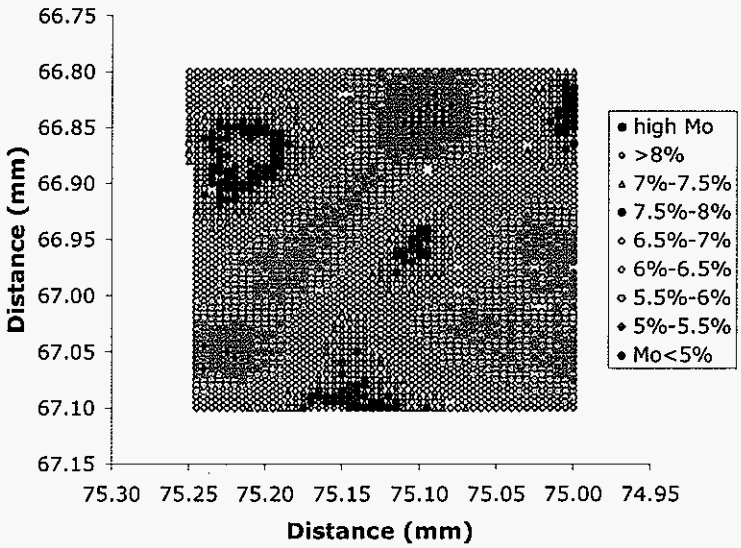

Figure 33 WDS map of Mo concentration of a CN3MN solution heat treated sample where the high concentration of Mo corresponds to the interdentritic regions

5.2.2. Phase Transformation Behavior

Metallographic examination of CN3MN showed that σ and Laves nucleated at longer times than for CK3MCuN. At 900°C, the microstructure seems to be completely σ for all times greater than 1000 hours. Experimental volume percentage data for σ and Laves with

error bars of one standard deviation are presented with best fit-curves in Figure 34 and 35, respectively. It is apparent that the σ volume percent will continue to increase after 2040 hours at all temperatures. The Laves phase dissolved at 800 and 900°C after 1000 and 10 hours with maximum volume percents of 5.3 and 6.6%, respectively. The high amount of error associated with the volume percent measurements was a direct result of the macrosegregation discussed in 5.2.1.

Thermo-Calc was used once again in an attempt to predict equilibrium phases and volume percentages as a function of temperature, as presented in Figure 36. The σ phase was the only intermetallic predicted at equilibrium. This would be in agreement if Laves was metastable and dissolved to give way to σ formation. However, a large amount of ferrite is still being predicted for a system known to have a purely austenitic matrix. The incomplete experimental volume percentage results leave uncertainty as to whether the volume percents as predicted by *Thermo-Calc* are accurate. Therefore, as with CK3MCuN, these predictions were omitted from the final analysis.

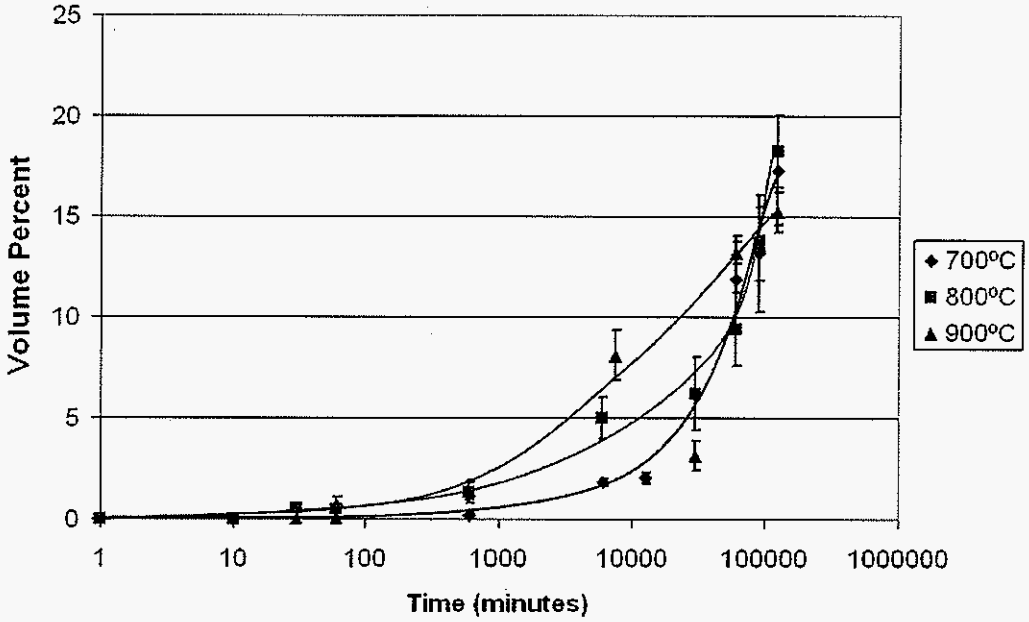

Figure 34 Experimental σ volume percents and best fit curve for CN3MN

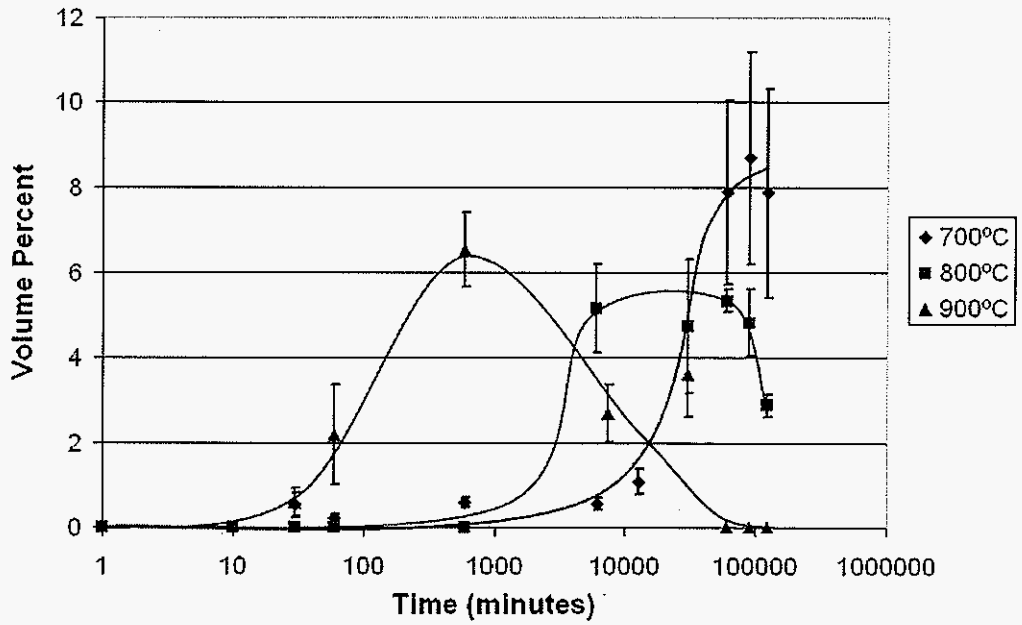

Figure 35 Experimental Laves volume percents and best fit curve for CN3MN

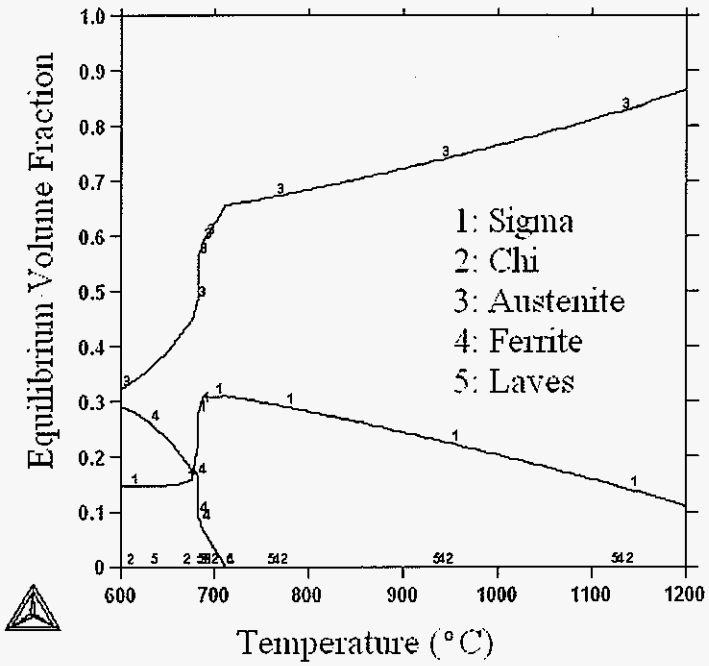

Figure 36 Equilibrium phases and volume fractions as calculated with *Thermo-Calc* for CN3MN

The number densities were calculated for CN3MN. The error was once again high due to macrosegregation and finer precipitates. The volume percentages and number densities for σ and Laves at 700, 800, and 900°C are presented in Figures 37, 39, and 41, respectively. Number densities were measured as the number of precipitates per $0.01mm^2$ and are graphed with one standard deviation error bars. Microstructures that correspond to these models are presented in Figures 38, 40, and 42. The micrographs were taken at varying magnifications due to macrosegregation effects and the vast differences in particle size as time increased. As seen in CK3MCuN, both σ and Laves precipitates found along the interdendritic boundaries and near voids are much larger than precipitates found within the dendrites. Also, the average precipitate sizes are displayed larger than the actual sizes where

only interdendritic boundary nucleation is present since the image analysis software counted an interdendritic boundary as one continuous precipitate.

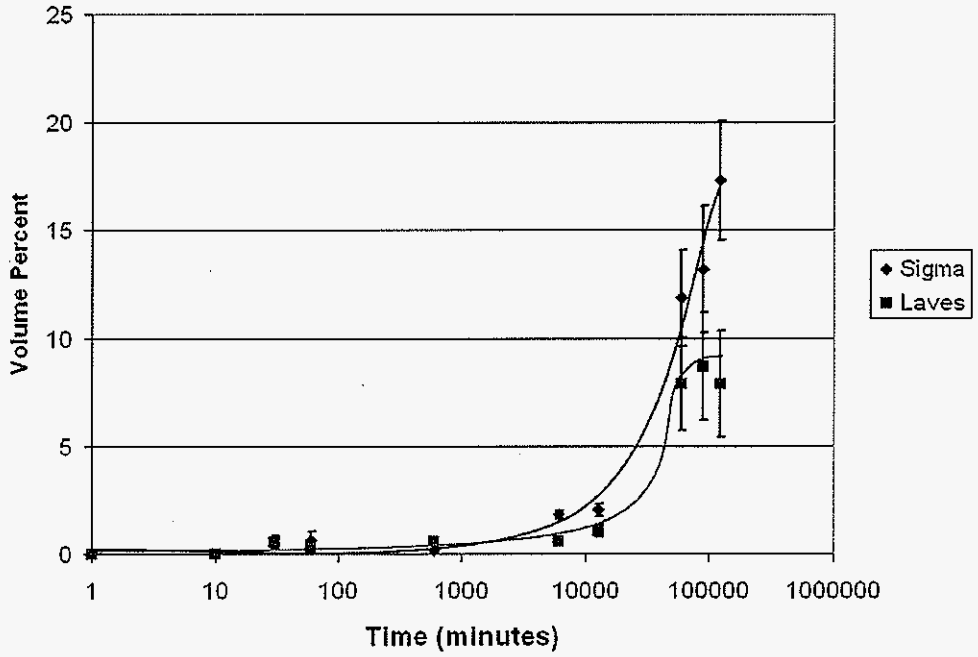

a)

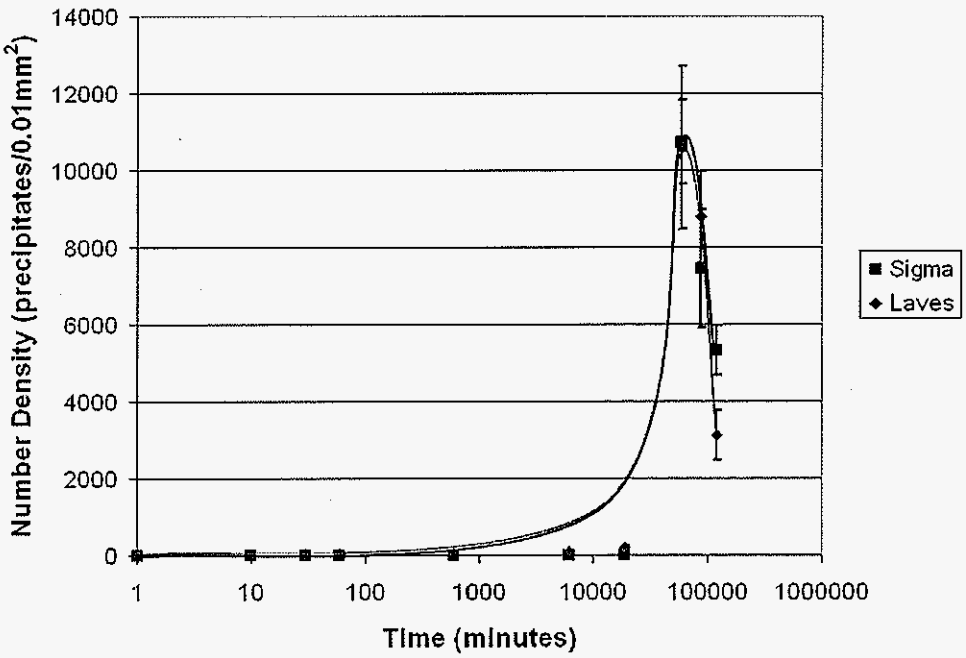

b)

Figure 37 Volume percents (a) and number densities (b) of σ and Laves at 700°C in CN3MN

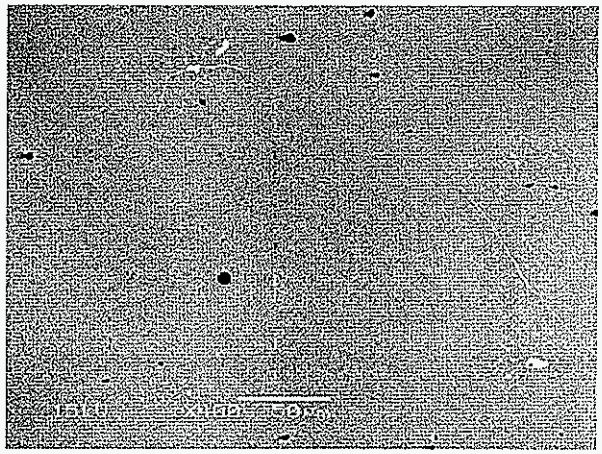

(a)

Average particle size of σ: 22.7μm^2 Laves: 1.88μm^2

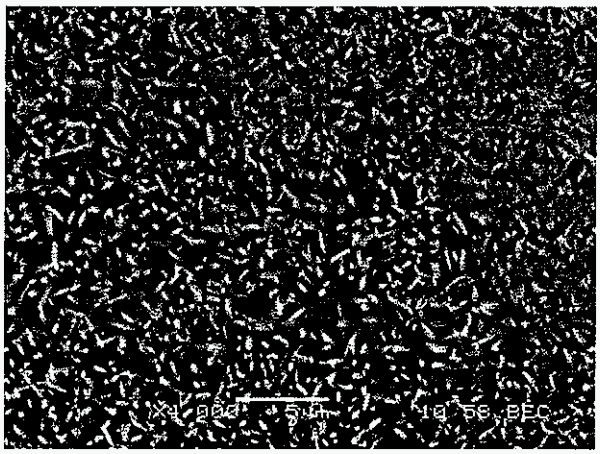

(b)

Average particle size of σ: 0.11μm^2 Laves: 0.07μm^2

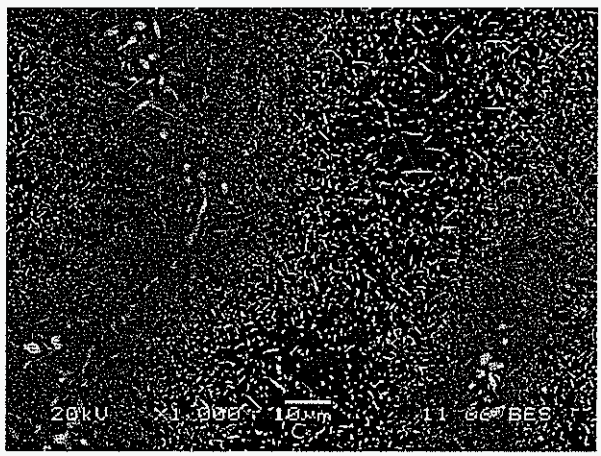

(c)

Average particle size of σ: 0.32μm^2 Laves: 0.25 μm^2

Figure 38 BSE images of CN3MN at 700°C for (a) 30 min (b) 1000 hours (c) 2040 hours

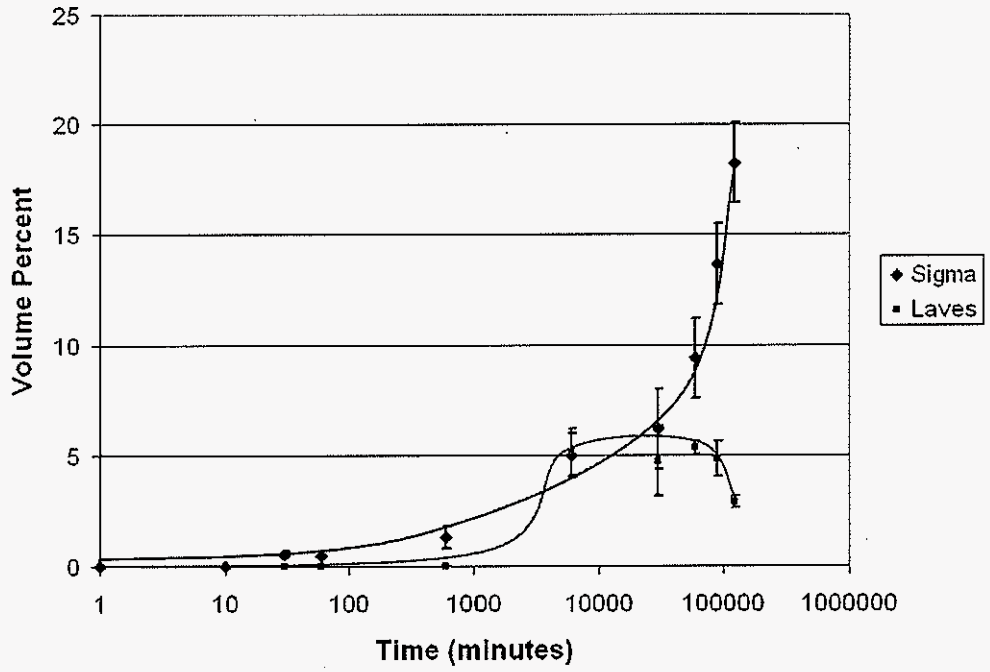

a)

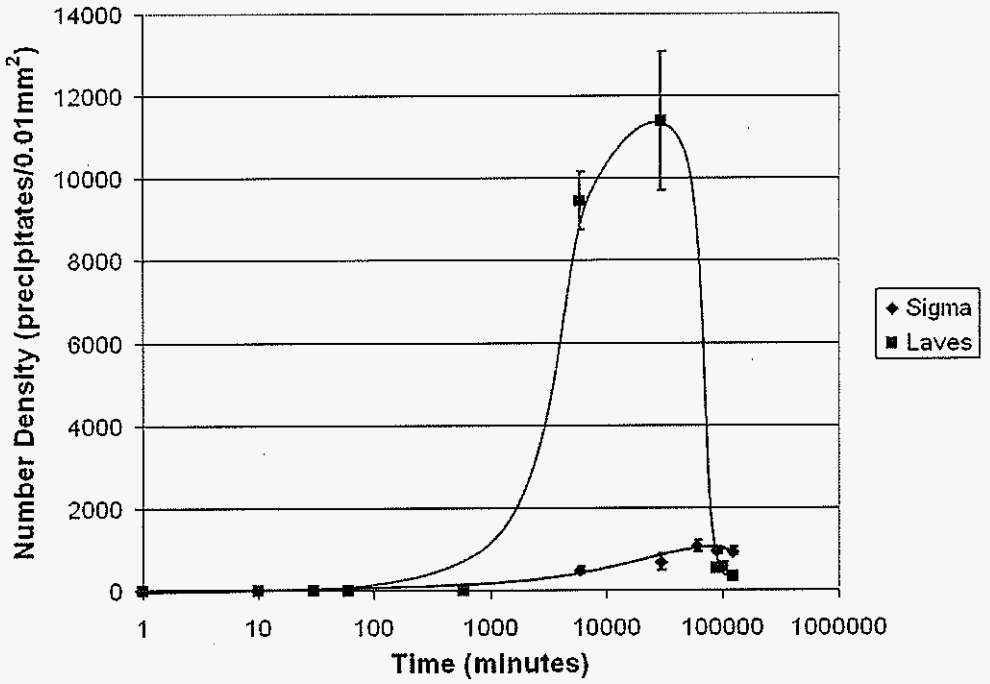

b)

Figure 39 Volume percents (top) and number densities (bottom) of σ and Laves at 800°C in CN3MN

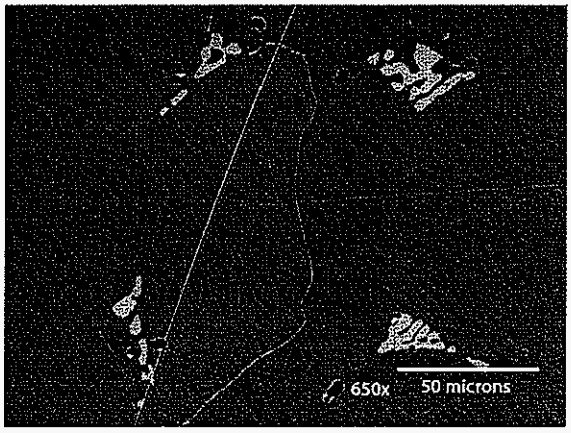

(a)
Average particle size of σ: 27.4μm^2

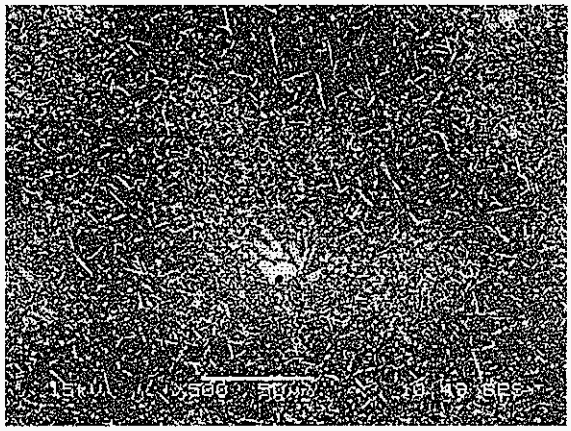

(b)
Average particle size of σ: 0.88μm^2 Laves: 0.97μm^2

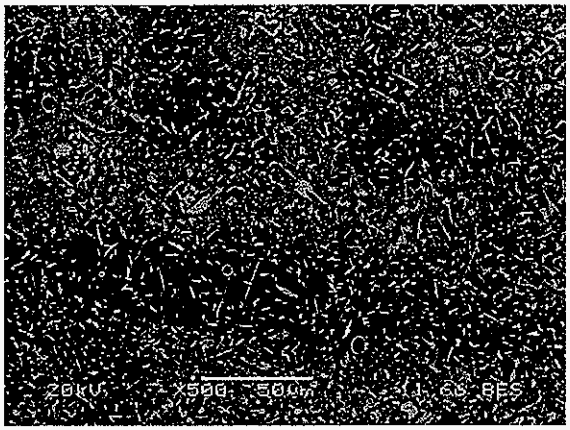

(c)
Average particle size of σ: 1.94μm^2 Laves: 0.88μm^2

Figure 40 BSE images of CN3MN at 800°C for (a) 10 hours (b) 1000 hours (c) 2040 hours

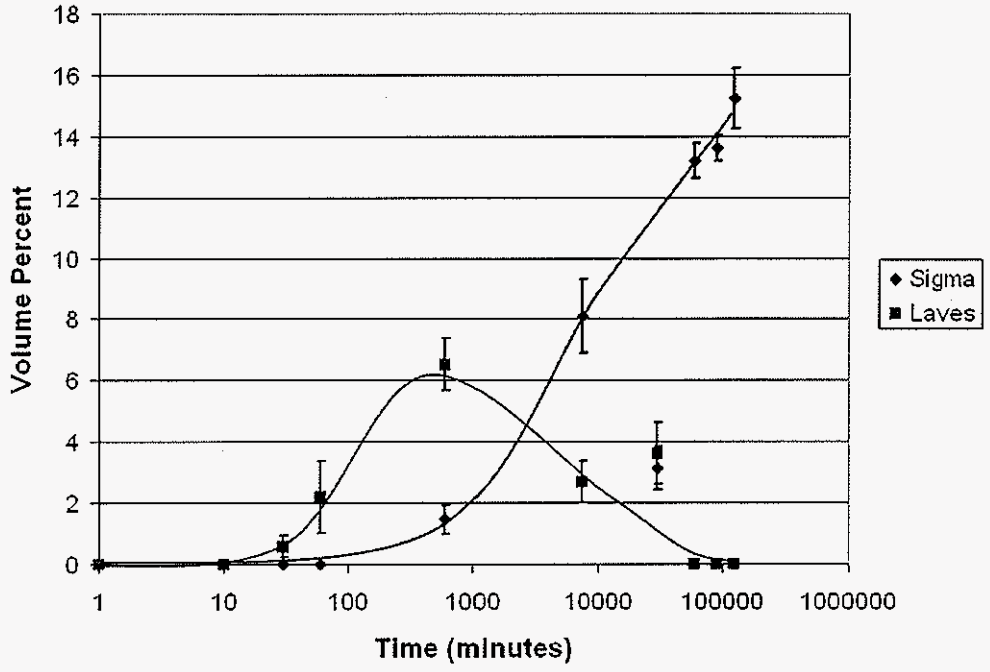

a)

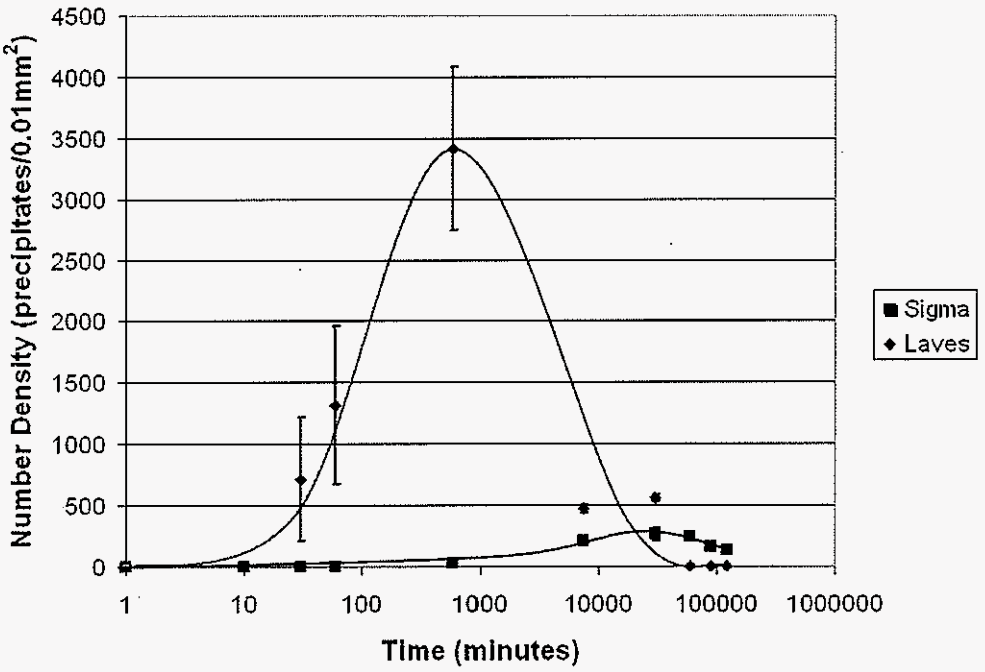

b)

Figure 41 Volume percents (a) and number densities (b) of σ and Laves at 900°C in CN3MN

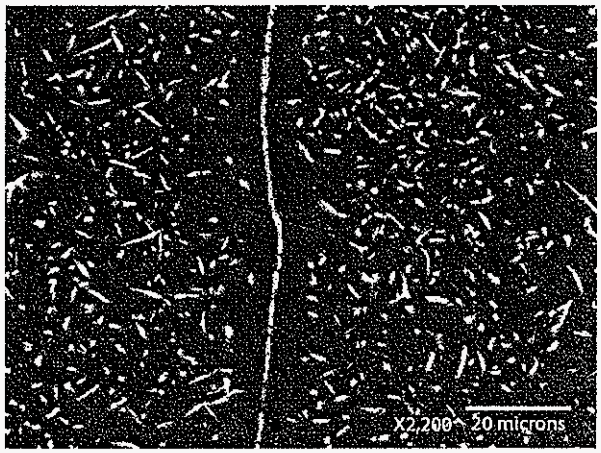

(a)

Average particle size of σ: 5.28μm^2 (large precipitates not shown) Laves: 0.19μm^2

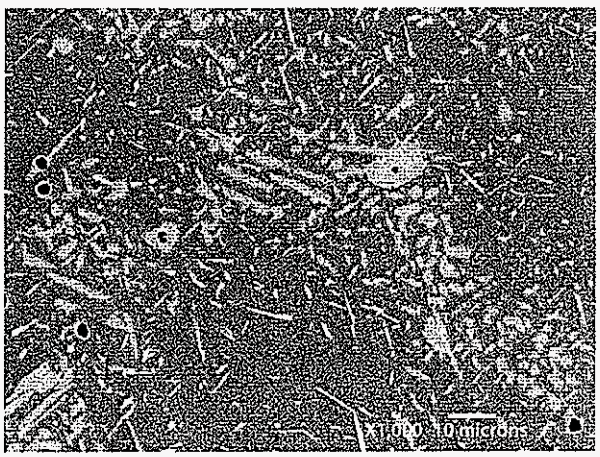

(b)

Average particle size of σ: 3.90μm^2 Laves: 0.57μm^2

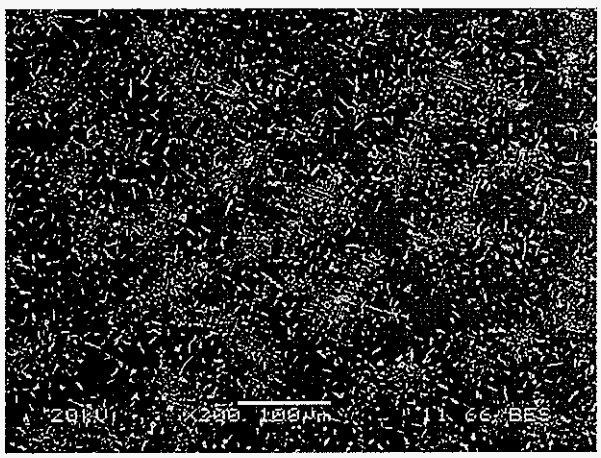

(c)

Average particle size of σ: 11.3μm^2

Figure 42 BSE images of CN3MN at 900°C for (a) 10 hours (b) 125 hours (c) 2040 hours

CHAPTER 6: DISCUSSION

6.1 Phase Transformation Analysis

6.1.1. Microstructure Evolution

A general sequence of the phase transformations seen at all temperatures in CK3MCuN and CN3MN is presented in Figures 43a-f and 44a-f, respectively. The size scale of the precipitates is not accurate for all temperatures, but gives a general understanding of how the phases nucleate, grow, and coarsen as time increases. The microstructures for both alloys showed similar behavior at short heat treatment times at all temperatures. However, due to segregation of Mo in CN3MN, the microstructures were very different for longer heat treatment times. The σ phase initially formed along interdendritic boundaries and near voids for both alloys. Larger precipitates often formed in these areas, similar to what is seen in Figure 43b. There was a small amount (<0.5 %) σ precipitation in the as-solution heat treated structure for CK3MCuN; whereas, it took between 30 to 60 minutes for σ to nucleate in CN3MN. Laves formation apparently followed that of σ in the interdendritic boundaries and near voids.

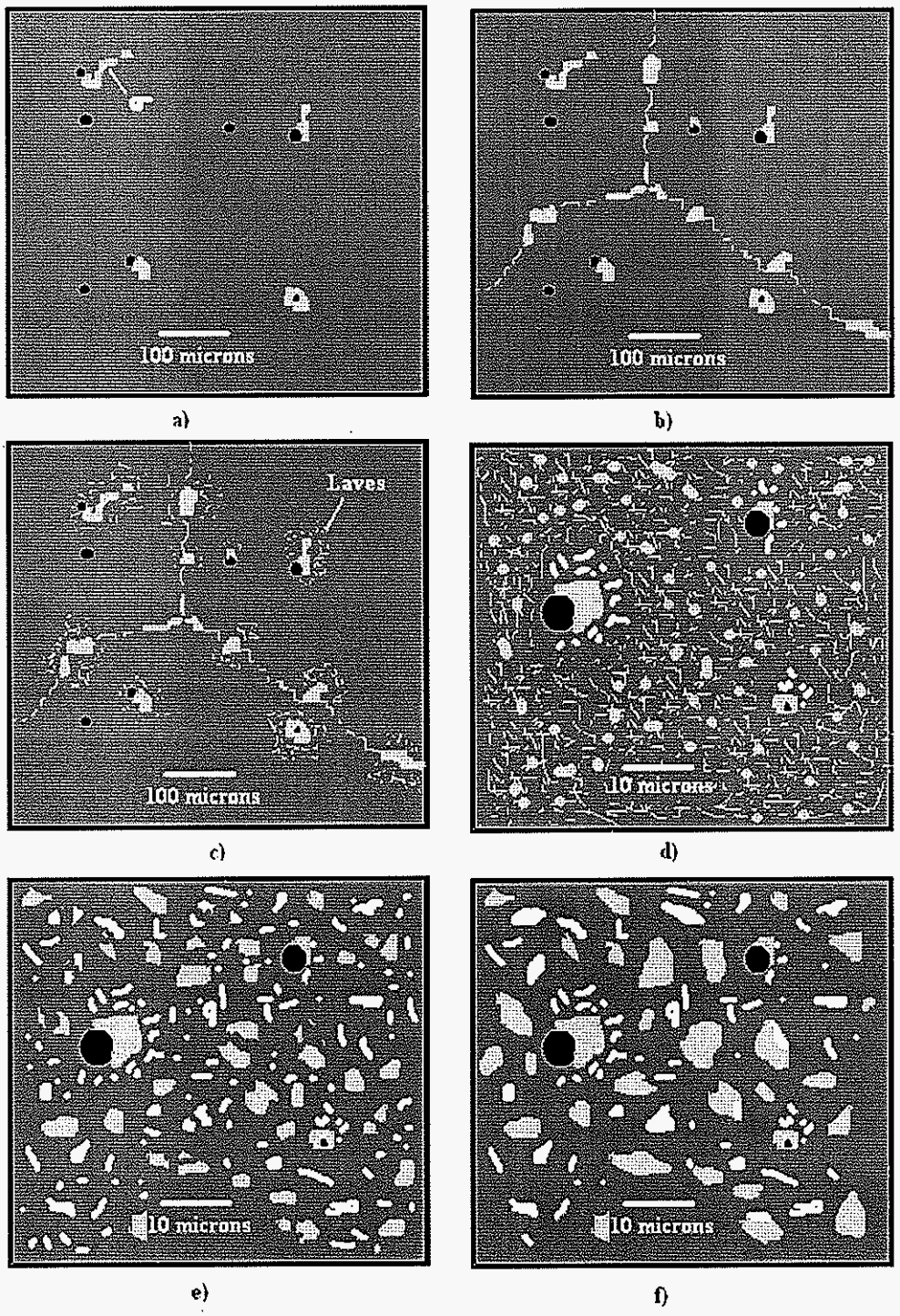

Figure 43 Microstructure evolution of CK3MCuN as time increases (gray phase: σ white phase: Laves)

a) As-solution heat treated with σ near voids b) σ along interdentritic boundaries c) Laves around interdentritic σ d) Fine σ and Laves within grains at higher magnification e) Growth of intragranular σ and Laves f) Growth and coarsening of intragranular σ and dissolution of Laves

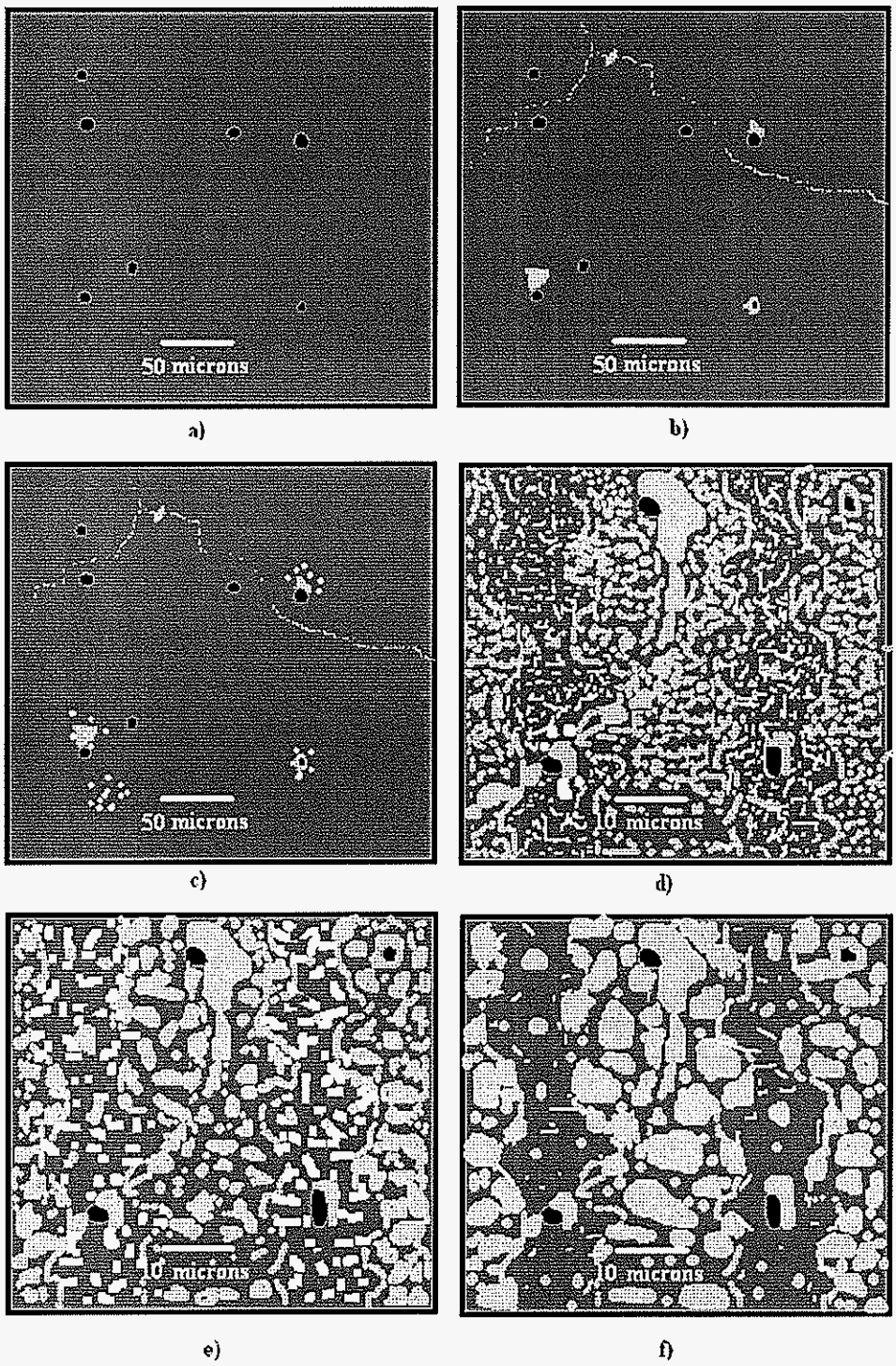

Figure 44 Microstructure evolution of CN3MN as time increases (gray phase: σ white phase: Laves)

a) As-solution heat treated structure b) along interdentritic boundaries and near voids c) Intragranular Laves around σ near voids d) Fine Laves in intradentritic regions and fine σ in interdentritic regions e) Growth of σ and Laves f) Growth and coarsening of σ and dissolution of Laves

Intradendritic precipitation of very fine needle-like Laves always followed Laves precipitation near the σ along the interdendritic boundaries and near voids. The Laves particles that surrounded the σ on the interdendritic boundaries were always larger than the Laves particles that nucleated within the dendrites, away from the interdendritic boundaries. Fine intradendritic σ precipitation usually followed the intradendritic precipitation of Laves. These former precipitates were more spherical than the intradendritic Laves. Similar to Laves, the intradendritic σ precipitates were much smaller in size compared to the σ found along the interdendritic boundaries and near voids. This was why the average size of the particles was very high for short times and dropped off as σ and Laves started to nucleate within the grains. Once growth and coarsening of both phases commenced, the average size also started to increase. In CN3MN, Laves was only seen in the interdendritic regions, where the high amounts of Mo segregation occurred. The intradentritic σ that nucleated in this alloy was in greater amount than in the interdendritic regions. At longer times (≥500 hours), Laves was seen to nucleate on the σ throughout both alloys.

The maximum size of Laves particles was much larger in CK3MCuN than in CN3MN at all temperatures. The Laves precipitates in CK3MCuN became more spherical as time progressed, while they remained needle-like at all times in CN3MN. After the Laves reached a certain maximum amount, it started to dissolve back into solution. This was evident at all temperatures for CK3MCuN and at 800 and 900°C in CN3MN. Laves dissolved completely at 900°C for CN3MN. The maximum size of a Laves precipitate before it dissolved was never as large as the σ precipitation for the same time and temperature.

Differentiation between σ and Laves based on contrast using backscattered electrons was more uncertain for samples aged at intermediate times and lower temperatures since

small Laves precipitates that might normally appear white due to atomic number contrast could appear gray due to beam spreading effects. Thus, the errors associated with the calculation of volume percents, number densities, and average particle sizes were greater for the heat treatments where the contrast was not as high (i.e. intermediate times and lower temperatures).

6.1.2. Volume Percents and Number Densities

The volume percent determinations, as presented in Figures 20 and 34, reveal that the time needed to start nucleating σ along the interdendritic boundaries is much shorter in CK3MCuN than in CN3MN. However, the overall time required to nucleate σ intragranularly before it started to grow appeared to be shorter in CN3MN than CK3MCuN. Growth started after 10 hours at all temperatures in CN3MN. Similarly, growth started after 10 hours at 900°C in CK3MCuN, but did not start until after 100 hours at 700 and 800°C. The rates at which σ grew in the two alloys were vastly different. In CK3MCuN, the σ volume percents apparently started to reach equilibrium at 900°C after about 500 hours; whereas, the volume percents are still growing at 700 and 800°C up to the maximum heat treatment time of 2040 hours. The σ volume percents in CN3MN were still increasing at a steady rate up to 2040 hours at all temperatures.

The time needed to nucleate Laves was similar at 700 and 900°C in both alloys, as seen in Figures 21 and 35. However, at 800°C the time needed to nucleate Laves was much longer in CK3MCuN. The time required to reach maximum growth at 900°C in CK3MCuN is much longer than in CN3MN, while the times were quite similar for both alloys at 800°C. However, Laves was still growing at 2040 hours at 700°C in CN3MN. An obvious

dissolution of Laves occurred at all temperatures in CK3MCuN, while dissolution was only seen at 800 and 900°C in CN3MN.

The number densities of both σ and Laves as a function of time for CK3MCuN of both σ and Laves reached a maximum, which would indicate the end of nucleation and the beginning of growth. For 700 and 800°C, the number densities reached a maximum and then decreased due, in part, to the start of coarsening of both phases. The number of Laves precipitates would also decrease as dissolution occurred. At 900°C, a similar maximum was seen for Laves; however, the growth of σ occurred over a range of times before starting to coarsen.

The number densities for CN3MN reveal that the number of Laves precipitates decreased at all temperatures, including 700°C, as time increased. The overall number of σ precipitates was much lower than the number of Laves precipitates at 800 and 900°C before dissolution occurs, even though the volume percents of σ were higher for the same times. Thus, the average size of a Laves particle was much smaller than the average size of a σ particle at all times. The number density of σ also appeared to increase at the same time the number density of Laves decreased at 800 and 900°C. This would suggest that σ nucleation was a direct result of the Laves dissolution.

Based on the results from the volume percents and number densities of σ and Laves, several conclusions can be made. First, the system preferentially forms σ at longer times and, therefore σ is considered to be the stable phase. Laves is considered to be a metastable phase in these systems since it dissolved into solution partially at most temperatures and completely at 900°C in CN3MN. Metastability in this case assumes that a driving force for formation exists at the temperatures of interest, but the magnitude of that driving force is lower than

what exists for the stable phase (i.e. σ). It is assumed that Laves eventually dissolved, completely or partly, into solution at all temperatures. It is possible for Laves to come to an equilibrium state at temperatures where complete dissolution was not observed.

The fact that the number density of σ reached a maximum would lead to the conclusion that that the system was at equilibrium. However, the volume percents were increasing at all temperatures and times at which the number density suggests equilibrium had been reached. Therefore, it is possible that growth and coarsening of σ were occurring concurrently due to local composition differences. This is especially the case in CN3MN where σ was at a lower amount in the interdendritic regions due to macrosegregation of Mo. The favored formation of σ eventually causes the Laves to dissolve. The Cr and Mo provided by the Laves dissolution would diffuse towards the σ in the interdendritic regions and cause further growth of this phase. However, the dendritic regions may have reached uniform compositions locally, thus mitigating further growth and signaling the start of coarsening. This may be the reason why the growth of σ in CN3MN took much longer than in CK3MCuN. Also, the number densities were much larger and average particle sizes much smaller for Laves in CN3MN than in CK3MCuN. This suggests that Laves did not coarsen as much in CN3MN as in CK3MCuN.

6.2. Transformation Kinetics

As discussed in section 2.2.1.2., the nucleation rate is dependent on how fast critical-sized nuclei can receive an atom from the matrix and on the concentration of critical sized

nuclei. How fast an atom is received from the matrix is determined by the rate of diffusion and the surface area of the critical-sized nucleus. The critical nucleus size needed for nucleation requires a small surface energy and/or a large driving force. As discussed in section 2.2.1.2., the barrier to nucleation, ΔG^*, is proportional to (γ^3/G_v^2). As the driving force increases and the surface energy decreases, the nucleation rate will increase, as seen by Equation 11.

Based on the results presented, an inferred set of Gibb's molar free energy curves as a function of composition for the stable phases γ and σ and metastable Laves are presented in Figure 45. The composition of γ when it is in equilibrium with Laves and σ, is given by C_L and C_{eq}, respectively. It was observed that to σ nucleated first in both CK3MCuN and CN3MN along the interdentritic boundaries and near voids at all temperatures. Under these conditions, the γ-matrix is at some supersaturated composition C_o. Figure 46 shows that for a matrix at C_o, the minimum nuclei composition for Laves and σ would be C_1 and C_2, respectively, since it is at these compositions that the σ and Laves would first have negative driving forces for formation. This would suggest that the metastable Laves could form first, because the diffusion needed to reach C_1 is less than the diffusion needed reach C_2. However, the interdendritic boundaries provide paths for rapid diffusion compared to intradendritic regions, so that the former sites would favor the nucleation of the stable σ.

The local concentration of vacancies is expected to be higher in the vicinity of a heterogeneous site, such as a grain boundary, than in a homogeneous site. Moreover, the diffusion coefficient for a substitutionally diffusing metal atom will be greater where the concentration of vacancies is higher. Therefore, as the concentration of vacancies increases, the rate of diffusion increases. The concentration gradient between the matrix and a

heterogenous site, similar to what is presented in Figure 9, is also much higher than between the matrix and homogenous nucleation site, causing the overall flux of atoms to be greater for areas such as interdendritic boundaries and voids. Therefore, the diffusion rate metal atoms would be faster in the vicinity of interdendritic boundaries and voids than in intradendritic regions. The faster rate of diffusion would cause the system to form the stable σ phase along the interdendritic boundaries or near voids before metastable Laves forms intragranularly around the σ.

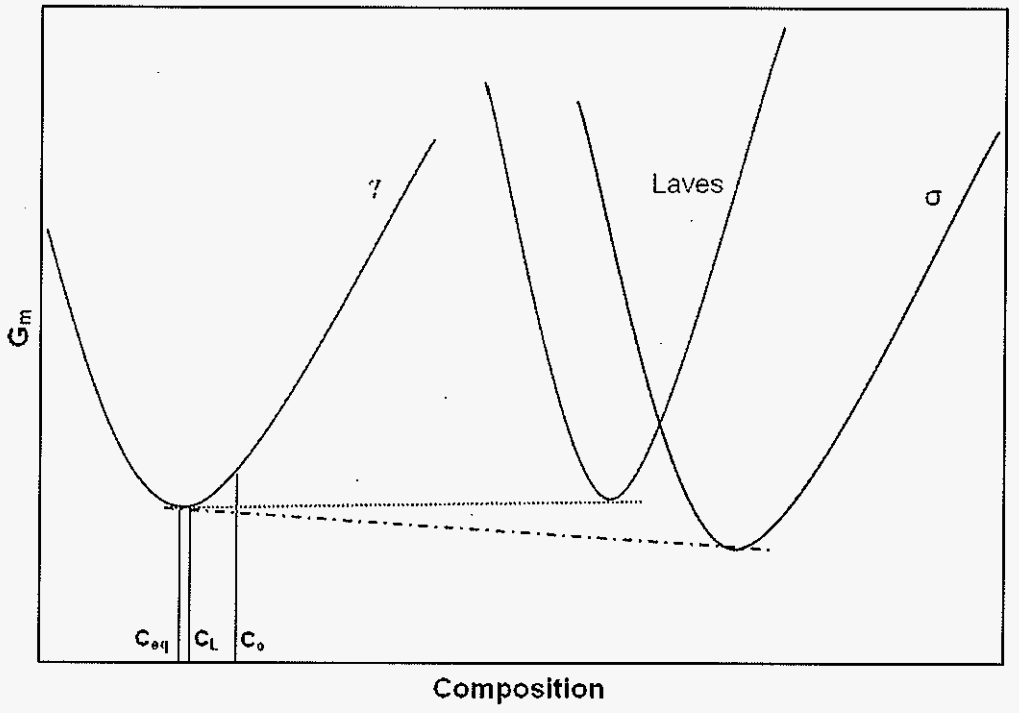

Figure 45 Molar Gibb's free energy curves at constant temperature showing the equilibrium conditions for σ and metastable Laves

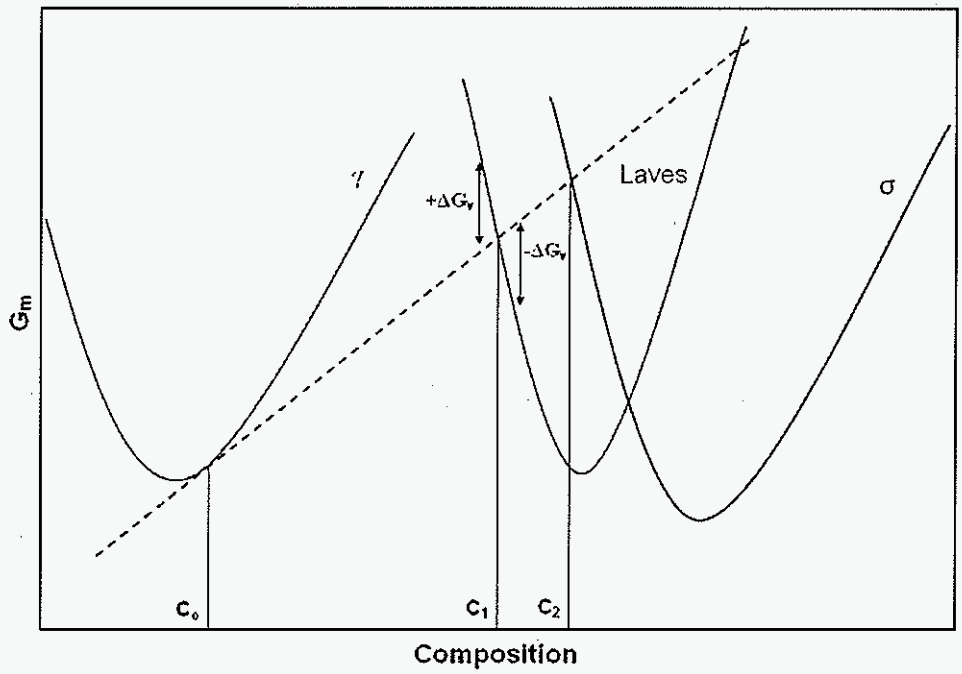

Figure 46 Molar Gibb's free energy curves at constant temperature showing the minimum concentration of σ and Laves nucleation for a system with composition C_o

Next, much finer Laves nucleates intradendritic in regions away from the interdendritic boundaries and voids. Intradendritic σ nucleates after Laves in similar regions. While the driving forces of σ and Laves may be only slightly different, the nucleation rate of the Laves phase appears to be equally as fast or faster than σ at all temperatures for both alloys. This is believed to be a result of the interfacial energy between the matrix and precipitate nuclei being less for the γ/Laves interface than the γ/σ interface. The interfacial energy between FCC- γ and HCP-Laves is assumed to be much lower than between FCC- γ and BCT- σ, since FCC and HCP are both closed-packed crystallographic structures. The (0001) and (111) are both closed pack planes with atomic packing factors of 0.74.

Svoboda et al.[3] also attributed the earlier formation of Laves to a suspected orientation relationship between γ and Laves. These authors reported on the free energy

differences between austenite and various decomposition products for the wrought alloy Avesta 654 (Fe-24.4Cr-21.9Ni-7.3Mo-3.65Mn-0.5N) at 700°C, as predicted by the thermodynamic and kinetic program, JmatPro. As shown in Table XI, the free energy difference for the formation of austenite + Laves is slightly less than the free energy difference for the formation of austenite + Laves + σ. The expected volume percents at 700°C are also predicted for the same decompositions. The expected volume percents of Laves at 700°C match well with the experimental results for Laves in CN3MN (Figure 35).

Table XI Free energy differences between austenite and various decomposition products and expected volume percents of Laves at 700°C as predicted by JmatPro[3]

Decomposition Reaction	ΔG, J/mol	Expected vol. % of Laves
$\gamma \rightarrow \gamma$ + Laves	-148	12%
$\gamma \rightarrow \gamma$ + Laves + σ	-223	8-10%

Since both σ and Laves are rich in Cr and Mo, they were competitively growing against one another. The growth rates of σ and Laves depend on the diffusion of Mo and Cr through the γ matrix and the surface energy associated with each precipitate. The maximum size of a Laves precipitate before it dissolves was never as large as the maximum size of a σ precipitate. Since Laves is high in Mo, it can be assumed that the diffusion of Mo was very slow in Laves formation. The Laves phase, as mentioned previously, was energetically favored to nucleate intragranularly first due to lower interfacial energy between the matrix and Laves nuclei. The formation of Laves would decrease the availability of Cr and Mo for σ formation and growth, in the early stages. However after σ nucleates and starts to grow, the average size of the spherical-like σ particles are much larger than the needle-like Laves particles.

The dissolution of Laves after it reached a maximum amount led to further growth of σ. The equilibrium driving force of σ is larger than the metastable equilibrium driving force of Laves, as shown in Figure 45, which causes the system to favor the formation of σ. The number densities of σ started to increase at higher rates as the Laves started to dissolve, as seen at higher temperatures. Therefore, local composition differences would occur in areas where σ is at equilibrium, causing it to coarsen, and areas where it is growing, due to the dissolution of Laves.

The dependence of σ formation on Laves dissolution in CN3MN can also be described by such a phenomenon. As the system approaches equilibrium, the Cr and Mo would have much further to diffuse to the σ in the intradendritic regions than if the Laves and σ were growing together in the same regions, as seen in CK3MCuN. This explains why the growth of the σ is much slower in CN3MN than CK3MCuN. This would also explain the local composition differences causing growth and coarsening to occur simultaneously.

CHAPTER 7: GENERAL CONCLUSIONS

The following conclusions were made based on the findings in this study.

1. The transformation kinetics of both CN3MN and CK3MCuN were extremely sluggish. Equilibrium conditions were not reached in either alloy after 2040 hour at 700 to 900°C. The transformations occurred fastest at 900°C, indicating the maximum transformation rate could be at temperatures higher than 900°C.

2. Backscattered electron SEM images revealed an obvious contrast between two intermetallics and the austenitic matrix. This allowed micrographs to be taken to determine volume percents and number densities of the two precipitates. Phase identification was done with TEM to reveal BCT- σ and HCP-Laves phases.

3. The intermetallic phases σ and Laves formed at all temperatures studied in both alloys. The high-Cr plate-like σ first formed along the interdendritic boundaries and near voids. Shortly thereafter, the needle-like Laves formed intradendritically around the σ. Laves continued to nucleate within the dendrites and σ shortly followed. A high degree of macrosegregation of Mo was seen in CN3MN. Laves formed only in high-Mo interdendritic regions, while higher σ amounts were found in the intradendritic regions than in interdendritic regions. The metastable Laves phase started to dissolve shortly after reaching a maximum transformation amount, which was never more than 10 vol. %. The stable σ phase continued to grow at the maximum heat treatment time of 2040 hours at all temperatures in

CN3MN and at 700 and 800°C in CK3MCuN. The σ at 900°C in CK3MCuN stabilized at approximately 12 vol. %.

4. The nucleation and growth rate of σ was much slower than the Laves, possibly due to a crystallographic orientation relationship between the HCP-Laves and FCC-austenite. The nucleation and growth rate of Laves in CN3MN was much faster at 800 and 900°C than in CK3MCuN. The nucleation rate of σ was also much faster in CN3MN; however, the growth rate was slower. The slow growth rate can be attributed to the segregation of Mo in the interdendritic regions, which made the formation of Laves preferential. Once the Laves dissolved, the Cr and Mo had a much longer distance to diffuse to the σ than in CK3MCuN. The macrosegregation of Mo seen in CN3MN could have been avoided if the as-cast bars were solution heat treated at temperatures and times that allowed for complete dissolution of Mo.

5. Number density calculations showed a maximum amount of σ precipitation and then an obvious drop off, indicating coarsening was occurring. However, the volume percents were still increasing for the same times where coarsening was observed. This indicated that growth and coarsening of σ were occurring simultaneously. This phenomenon is assumed to be a result of local compositional differences. Such measurements were not possible due to the spacing between σ precipitates being too small.

6. Inability to reach equilibrium conditions experimentally and inaccurate *Thermo-Calc* databases made the determination of TTT diagrams impossible, as the values of n and k in

the Avrami equation depend on the equilibrium volume percents at each isothermal temperature. It would be possible to reach equilibrium conditions if there was time to perform heat treatments for times longer than 2040 hours and at temperatures higher than 900°C.

REFERENCES

1. Stefan Heino, "Role of Mo and W during Sensitization of Superaustenitic Stainless Steel –Crystallography and Composition of Precipitates," *Metallurgical and Materials Transactions*, 31A (2000), 1893-2904

2. S. Heino, M. Knutson-Wedel and B Karlsson, "Precipitation in High Nitrogen Superaustenitic Stainless Steel," *Trans Tech Publications Ltd.*, 2005

3. M. Svoboda, A. Kroupa, J. Soousek, J. Vrest'al, and P. Miodownik, "Phase Changes in Superaustenitic steels after long-term annealing," *Z Metallk*, 95 (2004), 1025-1030.

4. T-H. Lee, S-J Kim, and Y-C, Jung, "Crystallographic Details of Precipitates in Fe-22Cr-21Ni-6Mo-(N) Superaustenitic Stainless Steels Aged at 900°C," *Metallurgical and Metals Transactions*, 31A (2000), 1713-1723.

5. S. Heino, M. Knutson-Wedel, B. Karlsson, *Materials Science Forum,* 318-320 (1999), 143-148

6. Y.-J. Kim, L. S. Chumbley, B. Gleeson, "Development of Isothermal Transformation Diagrams for Sigma-Phase Formation in Cast Duplex Stainless Steels," *Steel Founders' Society of America 2003 T&O Conference*, submitted, 2003

7. M. Blair and R. Pankiw, "Cast Corrosion- and Heat-Resistant Alloys", Practical Handbook of Stainless Steels & Nickel Alloys, ASM International, Materials Park, OH, USA, 2000, 31-83

8. C. W. Kovach, "High-Performance Stainless Steels", Nickel Institute, Toronto, Ontario, Canada, 2000

9. I. A. Franson and J. F. Grubb, "Superaustenitic Stainless Steels", Practical Handbook of Stainless Steels & Nickel Alloys, ASM International, Materials Park, OH, USA, 2000, 243-285

10. J. R. Davis, ASM Specialty Handbook Stainless Steel, ASM International, Materials Park, OH, USA, 1994

11. D.A. Porter and K.E. Easterling, *Phase Transformations in Metals and Alloys, 2nd Edition* (Cheltenham, United Kingdom: Nelson Thornes Ltd, 2001)

12. Y-J. Kim, "Phase Transformations in cast duplex stainless steels" (Ph. D. Thesis, Iowa State University, 2004)

13. C. R. Barrett, W. D. Nix, A.S. Tetelman, "The Principles of Engineering Materials", Englewood Cliffs, NJ, Prentice-Hall, 1973

14. Y-J. Kim, L. S. Chumbley, B. Gleeson, "Development and Assessment of Isothermal Transformation Digrams for Sigma-Phase in Cast Duplex Stainless Steels CD3MN and CD3MWCuN," *Metallurgical and Materials Transactions*, 35A (2004) 3377-3386.

15. J. W. Christian, "The Theory of Transformations in Metals and Alloys, Part 1: Equilibrium and General Kinetic Theory", New York, NY, Pergamon, 1975, 2nd Ed.

16. N. Saunders, A. P. Miodownik, "CALPHAD (Calculation of Phase Diagrams), A Comprehensive Guide", Pergamon Materials Series, Oxford, UK, Elsevier, Vol.1, 1998.

17. G. Herbslab, *Werkstoffe und Korrosion*, 33, 334 (1982)

18. C. Bates, L. Tillery, *Atlas of Cast Corrosion-Resistant Alloy*, Steel Founders' Society of America, 1985

19. B. Sundman, B. Jansson, and J. –O. Andersson, *Calphad*, 9, 153 (2002)

20. J. L. Walter, M. R. Jackson, C. T. Sims (Ed.), "Alloying", Metals Park, OH, American Society of Metals, 1988.

21. R. W. K. Honeycombe, "Steels: Microstructure and Properties", Metals Park, Oh, American Society for Metals, 1981.

22. P. Shewmon, "Diffusion in Solids", Warrendale, PA, TMS, 1989, 2nd Ed.

23. J. D. Verhoeven, "Fundamentals of Physical Metallurgy", New York, NY, John Wiley and Sons, 1975.

24. B. C. Schaffernak, H. H. Cerjak, "Design of Improved Heat Resistant Materials by Use of Computational Thermodynamics", *Calphad*, 25, 241 (2001)

25. J. Miettinen, "Thermodynamic Description of Solution Phases of Systems Fe-Cr-Si and Fe-Ni-Si with Low Silicon Contents and with Applications to Stanless Steel", *Calphad*, 23, 249 (1999)

26. B. D. Cullity, E*lements of X-Ray Diffraction, 2nd Edition.* (Reading Massachusetts: Addison-Wesley Publishing Company, Inc., 1978)

27. I. J. Polmear, *Light Alloys: Metallurgy of the Light Metals, 3rd Edition.* (New York, New York: Halsted Press, 1996). 27-31

28. C. V. Thompson, "On the role of diffusion in phase selection during reaction at interfaces", *J. Mater. Res.*, 7, 367 (1992)

29. J. D. Robson and H. K. D. H. Bhadeshia, "Modelling precipitation sequences in power plant steels: Part 1 - Kenetic theory", *Materials Science and Technology*, 13, 631 (1997)

30. A. Schneider and G. Inden, "Simulation of the kinetics of precipitation reactions in ferritic steels", *Acta Materialia*, 53, 519 (2005)

ACKNOWLEDGEMENTS

This work was funded by the United States Department of, and was in collaboration with the Steel Founders' Society of America (SFSA), the John Deere Technology Center, Allegheney Ludlum, Southwest Steel Casting, Inc., ANCAST, and Keokuk Steel Castings. This work was performed at Ames Laboratory under contract no. W-7405-Eng-82 with the US Department of Energy and Iowa State University. The United States government has assigned the DOE Report number IS-T 2662 to this thesis. The author would like to thank his Co-Major Professors, Dr. L. Scott Chumbley and Dr. Brian Gleeson, along with committee member Dr. Frank Peters. Special thanks also go to Dr. Chao Jiang, Alfred Kracher, Dr. Ozan Urgulu and Dr. Yoon-Jun Kim for assisting with this study. Also, I would like to thank my wonderful wife, Tami, other family members, and friends who have showed me never ending support throughout this project.